Collaborative Impact of Cryo-Treated Cutting Tool and Hybrid Milling Environment Towards Improved Sustainable Milling of ASTM F2063 Ni55.6Ti44.4 Alloy

Citation: Davis, Rahul, Singh, Abhishek, Pereira, Robson B. D., Sabino, Roberta M., Popat, Ketul et al. 2023. "Collaborative Impact of Cryo-Treated Cutting Tool and Hybrid Milling Environment Towards Improved Sustainable Milling of ASTM F2063 Ni55.6Ti44.4 Alloy."

As Published: https://doi.org/10.1007/s40684-023-00520-9

Publisher: Korean Society for Precision Engineering

Persistent URL: https://hdl.handle.net/1721.1/152931

Version: Author's final manuscript: final author's manuscript post peer review, without publisher's formatting or copy editing

ACCEPTED MANUSCRIPT

Collaborative Impact of Cryo-treated Cutting Tool and Hybrid Milling Environment towards Improved Sustainable Milling of ASTM F2063 Ni55.6Ti44.4 alloy

Cite this Accepted Manuscript (AM) as: Accepted Manuscript (AM) version of Rahul Davis, Abhishek Singh, Bruno Robson, Pereira, Roberta Sabino, Ketul Popat, Paulo Soares and Lincoln Brandão, Collaborative Impact of Cryo-treated Cutting Tool and Hybrid Milling Environment towards Improved Sustainable Milling of ASTM F2063 Ni55.6Ti44.4 alloy, International Journal of Precision Engineering and Manufacturing-Green Technology https://doi.org/10.1007/s40684-023-00520-9

This Accepted Manuscript (AM) is a PDF file of the manuscript accepted for publication after peer review, when applicable, but does not reflect post-acceptance improvements, or any corrections. Use of this AM is subject to the publisher's embargo period and AM terms of use. Under no circumstances may this AM be shared or distributed under a Creative Commons or other form of open access license, nor may it be reformatted or enhanced, whether by the Author or third parties. By using this AM (for example, by accessing or downloading) you agree to abide by Springer Nature's terms of use for AM versions of subscription articles:
https://www.springernature.com/gp/open-research/policies/accepted-manuscript-terms

The Version of Record (VOR) of this article, as published and maintained by the publisher, is available online at: https://doi.org/10.1007/s40684-023-00520-9. The Version of Record is the version of the article after copy-editing and typesetting, and connected to open research data, open protocols, and open code where available. Any supplementary information can be found on the journal website, connected to the Version of Record.

For research integrity purposes it is best practice to cite the published Version of Record (VOR), where available (for example, see ICMJE's guidelines on overlapping publications). Where users do not have access to the VOR, any citation must clearly indicate that the reference is to an Accepted Manuscript (AM) version.

Accepted manuscript

Collaborative Impact of Cryo-treated Cutting Tool and Hybrid Milling Environment towards Improved Sustainable Milling of ASTM F2063 $Ni_{55.6}Ti_{44.4}$ alloy

Rahul Davis [1*], Abhishek Singh [2], Robson Bruno Dutra Pereira [3], Roberta Maia Sabino [4], Ketul Popat [5,6,7], Paulo Soares [8], Lincoln Cardoso Brandão [3]

[1] Department of Mechanical Engineering, Vaugh Institute of Agricultural Engineering and Technology, Sam Higginbottom University of Agriculture, Technology and Sciences, Prayagraj, 211007, India *rahul.davis@shiats.edu.in*, https://orcid.org/0000-0003-4795-9174

[2] Department of Mechanical Engineering, National Institute of Technology Patna, Patna, 800005, India. *abhishek.singh@nitp.ac.in*, https://orcid.org/0000-0002-0888-4694

[3] Department of Mechanical and Production Engineering, Centre for Innovation in Sustainable Manufacturing- CIMS, Federal University of São João del-Rei, São João del-Rei, Minas Gerais, Brazil
robsondutra@ufsj.edu.br, https://orcid.org/0000-0001-9080-8393,
lincoln@ufsj.edu.br, https://orcid.org/0000-0003-3897-2393

[4] Institute for Medical Engineering and Science, Massachusetts Institute of Technology, Cambridge, Massachusetts, United States of America
rsabino@mit.edu,https://orcid.org/0000-0001-5919-5314

[5] School of Advanced Materials Discovery, Colorado State University, Fort Collins, Colorado, United States of America
[6] School of Biomedical Engineering, Colorado State University, Fort Collins, Colorado, United States of America
[7] Department of Mechanical Engineering, Colorado State University, Fort Collins, Colorado, United States of America
ketul.popat@colostate.edu, http://orcid.org/0000-0002-2417-7789

[8] Department of Mechanical Engineering, Pontifícia Universidade Católica do Paraná, R. Imaculada Conceicao, Curitiba, PR, 80215 901, Brazil
pa.soares@pucpr.br, https://orcid.org/0000-0001-9325-8139

Corresponding author: [1*]*rahul.davis@shiats.edu.in*

Abstract: Shape memory alloys are mainly used in medical devices and surgical implants due to their biocompatibility. Machining these alloys into intricate patterns can be challenging due to their poor thermal conductivity which could lead to a poor surface finish. The poor surface finish causes a release of toxic elements such as Nickel, leading to contact allergies and thus deteriorating its biocompatibility. Using the right cooling technology can help improve their machinability and overcome issues related to surface integrity. The current study investigates the effect of milling parameters (cutting-speed, feed rate, and depth of cut) and different cooling strategies (flood coolant, cryogenic liquid nitrogen, and a hybrid approach) on the surface integrity of F2063 $Ni_{55.6}Ti_{44.4}$ shape memory alloy. In addition, the effect of cryogenically treating the cutting tool for further enhancement of surface finish was investigated. A considerable modification on the milled surfaces was observed when using the hybrid cooling/milling approach and cryo-treated tools in terms of morphological, chemical compositional, crystallographic, and microhardness. In addition, this modified surface had a noticeably improved bioactivity due to enhanced hydrophobicity (with contact angle 92°) and surface topography (Ra: 341.69 nm), which favoured cell adhesion and proliferation. The results indicate that the modified $Ni_{55.6}Ti_{44.4}$ alloy surface might be adequate for use in medical applications.

Keywords: Cryo-treated cutting tool; wet, cryo, and hybrid milling environment; ASTM F2063 $Ni_{55.6}Ti_{44.4}$ alloy; surface roughness; microhardness; bioactivity

1. Introduction

Over the last few decades, the productive collaboration among medical science, material science, and engineering has been constantly introducing some specific biologically compatible smart and/or novel materials to deal with physical sicknesses such as heart disease or fracture fixation/arthrodesis. One such category of lightweight smart biomaterials is nickel-titanium (NiTi) shape memory alloy (SMA), which was also termed "Nitinol" after the U.S. Ni-Ti-Naval Ordnance Laboratory. Nitinol is non-cytotoxic, tough, corrosion-resistant, and capable of changing its shape and operating at high temperatures. It is relatively less costly in comparison to Gold-Cadmium SMAs [1]. The superior biocompatibility and superelasticity of Nitinol amongst all SMAs make it suitable for use comfortably inside the human body for different biomedical purposes. The superelasticity of Nitinol in conjunction with high fatigue resistance makes it appropriate for application in varieties of non-degradable/permanent biomedical implants such as vascular stents, transcatheter heart valves, neurovascular clot pullers, and atrial fibrillation devices. In orthopedic applications such as osteotomy fixation and compression staples, unlike other titanium and stainless steel alloys, Nitinol's spontaneous recovery from a contorted shape, mechanobiological characteristics, and low-modulus (from its reverse phase transformation) enables a more uniform load distribution over the implant and bone and thus minimize the stress shielding of bone and chances of implant failure [2].

Nitinol exhibits phase transformation when subjected to a considerable variation in temperature or stress. High temperatures lead to cubic austenite with Young’s modulus ranging from 60 to 90 GPa, whereas low temperatures to monoclinic martensite with Young’s modulus ranging from 28 to 41 GP. However, Nitinol possessing relatively high Ni content may have R-phase. The start of the austenitic and martensitic phases is abbreviated as A_s and M_s, respectively, and similarly, their finish phases are as A_f and M_f, respectively. Additionally, the martensitic phase displays lower elastic modulus, magnetic susceptibility, and electrical resistivity compared to the austenitic phase [3]. Biomedical implants have complex shapes and designs. Acquiring these appreciable sizes and shapes on Nitinol via traditional manufacturing techniques is often strenuous due to its low machinability, substantial strain hardening, and deformation resistance. Consequently, the developed stresses and high temperatures during metal cutting induce the phase transformation in Nitinol. Moreover, the precise conversion of titanium (Ti) alloys including Nitinol into the desired form also depends on the proper selection of a suitable subtractive manufacturing process, input variables, and cooling environment in both traditional and non-traditional settings at both macro [4, 5] and micro-levels [6, 7]. However, as concluded by a comprehensive recent survey [8], in the case of traditional subtractive processing of nickel-titanium alloys, extensive studies are urgently required where cooling conditions and the cutting tools’ properties are significantly varied using advanced approaches. In this relation, a previous study highlighted a considerable role of low-temperature cooling agents (cryogenic coolants) such as the health-friendly liquid nitrogen (LN_2), as a potential cooling candidate for eliminating the high machining temperatures and reducing cutting forces, which could further lead to Nitinol’s phase transformation [9, 10]. However, this study presented only some preliminary findings. A recent study also reported the use of chilled air cooling amid the micro-milling of Nitinol, leading to an enhanced machinability in terms of improved phase transformation and chip thickness [11]. However, no such successful study in the case of macro-milling has been reported so far. Further, in the case of cryogenic cooling environments [12], the cryogenic coolant exhibited approximately 50 % liquid state when it hits the targeted spot, indicating an improved rate of heat transfer chiefly in the sub-cooled boiling region [13]. In this regard, the studies found that cryogenic coolant achieved a higher heat-transfer coefficient of the order of 20,000 W/m^2K in comparison to natural convection with an increased surface cooling rate [14]. A study conducted on Nitinol 60, reported a high resistance against corrosion and brittleness under cryogenic temperatures [15]. Also, it was demonstrated in some studies on Ti-alloys that the manufactured surfaces and cutting tools exhibited better surface integrity and lower tool wear, respectively, with LN_2 compared to minimum quantity lubrication (MQL) and dry machining conditions [16, 17]. This superiority of the potential of LN_2 was further verified in some investigations on degradable implant Mg alloys [18, 19]. However, since the present work aims at the non-degradable implant biomaterials, based on the research gap noticed in the previous research on cooling approaches incorporated while processing such materials, it was observed that some recent literature emphasized the frequent use of hybrid cooling/milling environments (simultaneous application of more than one coolant) such as LN_2 and MQL, CO_2 snow and

MQL, cutting fluid and LN_2 [20, 21], bio-based nano lubricants blend formulation comprising coconut oil, sodium dodecylbenzene sulfonate, Cocamidopropyl betaine CAPB with 0.5% of Al_2O_3 nanoparticles [22], and vegetable and mineral-based fluids (using MQL approach) [23] amid different material subtractive processes. In this relation, concerning the latest progress in achieving surface modification on metallic biomaterials using non-traditional approaches [6, 7], a few recent studies hybridized the cooling environment by combining the conventional cutting fluid and LN_2 and found its greatest impact when used with cryo-treated cutting tool in traditional milling of degradable magnesium (Mg) alloys AZ31B [24] and AZ91D [25], and non-degradable Ti-6Al-4V alloy [26]. These studies found that the untreated cutting tool displayed a better performance when used with LN_2, however, the cryo-treated cutting tool achieved superior outcomes in association with a hybrid cooling/milling environment. The fact of the remarkable performance of cryo-treated cutting lay in previous studies that reported a noteworthy effect of cryogenic treatment on the carbide cutting tool properties and performance, which can substantially reduce the softening, wear, dissociation, and consequent plucking of carbide grains, and deformation of the cutting tool amid machining [27, 28].

Previous literature projected cryogenic cooling assisted-traditional machining as a superior material subtraction technique of Nitinol over other cooling strategies. For instance, cryogenic machining induced a significant improvement in surface microhardness, phase transformation temperature, and strength of $Ni_{50}Ti_{50}$ alloy [10], reduced the progressive tool-wear amid turning of room temperature austenitic $Ni_{50.8}Ti_{49.2}$ alloy [29], enhanced tool wear and changed the phase from austenite to B19' martensite phase during machining of $Ni_{49.9}Ti_{50.1}$ alloy [30], and substantially altered the austenite finish temperature of martensitic of $Ni_{49.9}Ti_{50.1}$ alloy [31]. However, the employment of hybrid cooling/milling strategies amid the machining of biocompatible Nitinol leading to enhanced findings was rarely recorded [32]. Although the recent investigations indicated the substantial incorporation of cutting tools without any surface treatment amid dry, wet, and cryogenic machining of Nitinol, to the authors' knowledge, the inclusion of a cryo-treated cutting tool in association with hybrid cooling-assisted machining of Nitinol has not been reported till date. Consequently, the integration of a cryo-treated cutting tool with the low-temperature cooling environments and its succeeding influence on surface roughness, microhardness, and biocompatibility is still unstudied. Moreover, a large number of recent attempts in the above-mentioned comprehensive literature were noticed amid the cryogenic turning of Nitinol, whereas very limited studies were reported on the cryogenic milling of Nitinol. Hence, in the present context, a closer glance at the literature on modern cooling methods and cutting tool's surface treatment conditions in the subtractive manufacturing of Nitinol, however, reveals several research gaps. In this regard, the present research addresses the need for the advanced processing of Nitinol with a hybrid cooling strategy and cryo-treat cutting tool in the milling operation, so far lacking in the scientific literature. Also, in two studies, the nitinol surfaces machined by electric discharge machining (EDM) and zinc powder mixed-EDM, were detected with a considerably enhanced biological response of cells due to notably improved wetting behavior and topography, leading to a better cell attachment and even differentiation [7, 33]. However, studies outlining the enhanced bioactivity of traditionally machined Nitinol are hardly available. Therefore, for bridging this gap, this research reports an innovative experimental study on the end milling of Nitinol with an untreated and cryogenically treated (cryo-treated) cutting tool (end mill) amid wet, cryogenic, and hybrid cooling/milling environments. The experiments were designed and executed using an L_{27} orthogonal array. Further, the observed experimental findings were analyzed and validated via statistical analysis and morphological study. The later sections of the study incorporate a detailed analysis of the milled surfaces of interest by field emission scanning electron microscopy (FESEM), energy dispersive X-ray (EDS), X-ray diffraction (XRD), and differential scanning calorimetry (DSC). The last two sections of the study report a biocompatibility test of the milled surface of interest, followed by a comparative morphological study of the cryo-treated cutting tool used in different cooling/milling environments.

2. Research procedure

This section provides the details of experimental and measuring setups.

2.1 Experimental setup

According to recent research, some specific surface characteristics such as topographic properties, wetting features, and thickness of the surface's topmost layer, of a medical implant, primarily ascertain its functionality in a biological environment. Consequently, the implant and cells' interaction can be significantly impacted even by slight changes in any of the above-mentioned surface characteristics [34]. Further, an investigation outlined that at different levels of input variables, for instance, depth of cut (a_p), feed rate (f_z), cutting-speed (V_c), and cooling environment (env), a machining process can significantly enhance the topography and morphology of a biomaterial. The surface layers experiencing plastic deformation along with the inclination of grooves and ridges/valleys (toward the direction of machining) regulate the final topography of the processed surface, and thus, manage the migration of cell lines [26]. Further, a study revealed that even very small variations in the Ni elemental composition of Nitinol with 55 weight % Ni, could lead to noticeable changes in Nitinol's overall behavior. For instance, a rise in Ni content by 0.1 weight % could decrease the transformation temperature by more than 100 °C and raise the austenite yield strength notably [35]. Therefore, considering such properties of Nitinol, its A_f temperatures, when found between 0 °C – 20 °C, could lead to the display of superelasticity even at human body temperature (37 °C) [7]**.** Therefore, in the present research, attempts were made to achieve an enhanced milling-induced surface modification on an ASTM F2063 $Ni_{55.6}Ti_{44.4}$ alloy (Ni 55.6 %, Ti 44.4 %, C<0.02%, A_f:10-15 °C, annealed condition) workpiece, procured from ALB Materials Inc, Henderson, USA, for biomedical applications. Although a recent investigation reported a remarkable modification of this workpiece material via non-traditional micro-electric discharge machining using zinc powder [7], the traditional techniques are still challenged. Hence, in the present work, 6 mm aluminum titanium nitride-coated solid carbide end mill cutters (KYOCERA SGS/SER 1M Ti-NAMITE) were used in untreated and cryo-treated conditions to perform the required end milling operations for a predetermined cutting length of 50 mm on an MTAB XL CNC milling machine of bed size 360×132 mm. The end mill cutter was 75 mm long with 4 flutes (flue length: 25 mm), 30° helix angle, 3700 HV hardness, and 1100 ℃ thermal stability. Besides, Zed-plus water-soluble conventional cooling medium was used as a cutting fluid for wet cooling/milling (WME), whereas in cryogenic cooling/milling (CME), LN_2 was used (at a temperature of -196 ℃) with the assistance of an ELGi SS02 compressor. Hybrid cooling/milling (HME) comprised the concurrent use of cutting fluid and LN_2.

Further, Fig. 1 (a) presents the deep cryogenic treatment (DCT) of the cutting tool. In addition, based on the recommendations of the recent literature [36, 37], the deep cryogenic treatment of the cutting tool was preferred over the shallow type since the former outperformed the latter in terms of superior hardness, thermal conductivity (assisting in a better heat-dissipation), uniformity in the formation of η-carbides, and thus better cutting tool life. This process involved the holding (soaking) of the cutting tool for 24 hours in a Cryogem-PS-34 container with a 1 °C/min rate of ramping down/cooling (to avoid the development of microcracks as a result of sudden cooling) up to -196 °C temperature in the atmosphere of LN_2. Once the cutting tool crosses the holding zone, its temperature is ramped up to the tempering temperature at the same rate. Besides, with the assistance of a recent review on the development of hybrid machining setups [38], the present research demonstrates the experimental configuration consisting of a milling machine, LN_2 dispensation arrangement, compressor, computer system, and a close view of the cutting tool with liquid coolant (cutting fluid) and LN_2 outlets in Fig. 1 (b). The authors have used the same milling setup in two of their previous studies performed on Mg alloy AZ31B [24] and Ti-6Al-4V alloy [26]. Fig. 1 (c) and (d) display the close look and top view, respectively, of the end mill cutting tool. Additionally, the recent literature also reported a considerable influence of direction, pressure, flow rate, and nozzle size through which a liquid coolant finally achieves its dispensation on the control of the generated high heat (due to friction among cutting tool, workpiece, and chips), and thus on the produced surface quality [26, 39, 40]. Hence, in the present research, the nozzles carrying cutting fluid and LN_2, respectively, were set at specific positions/angles with a stand-off distance of 15 mm away from the end mill's periphery that influenced the outcome most potentially during some preliminary tests. In the case of wet milling, the nozzle face was towards the milling region at an angle of 120° to the feed direction and 60° towards the horizon (to diminish the resistance between the end mill rake and chips interface). Whereas the nozzle faced the end mill at an angle of 90° to the feed direction and 30° towards the horizon in the case of cryogenic milling (to substantially decrease the heat at the end mill's cutting edge). The details of the same are shown in Fig. 1(e)-(h).

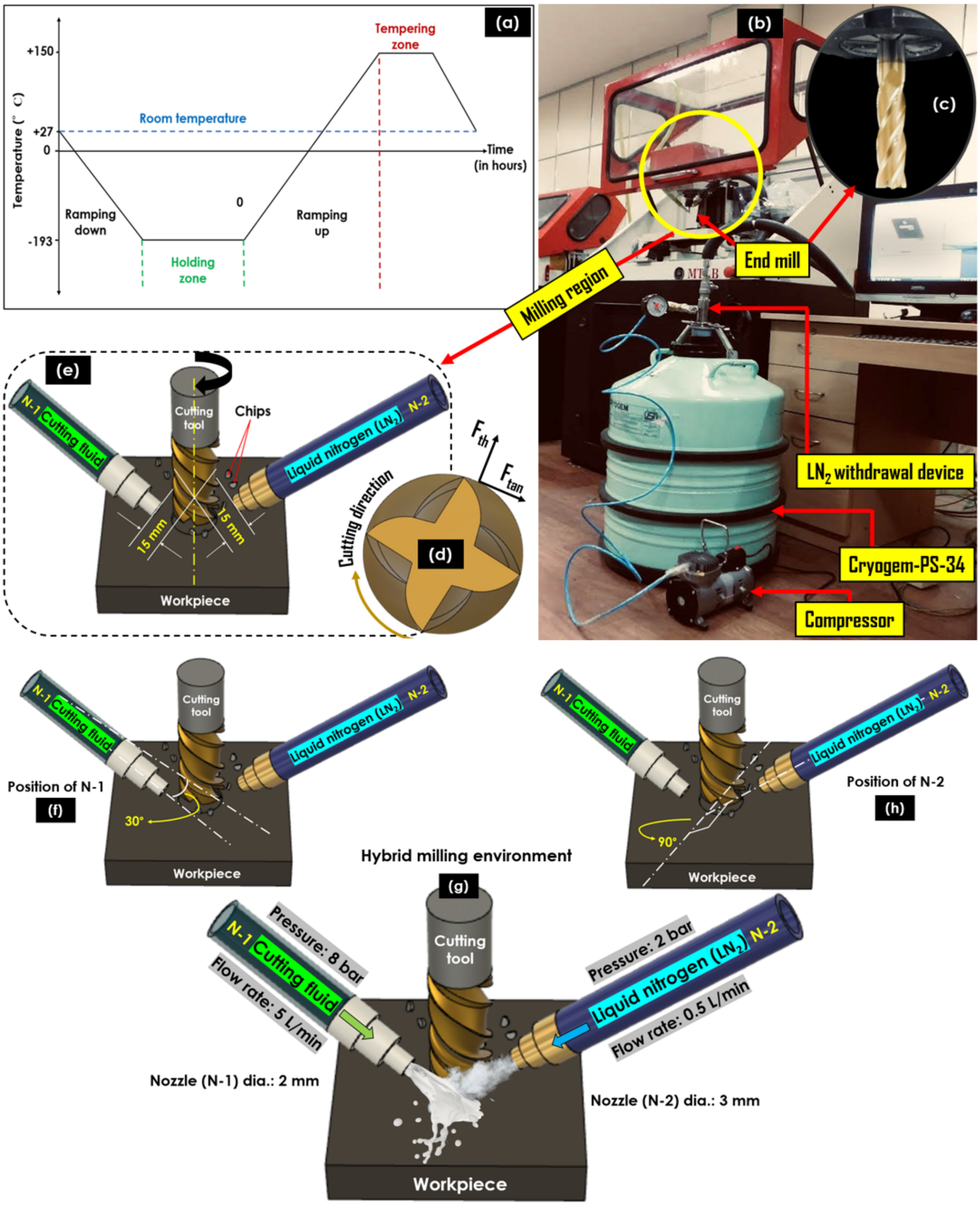

Fig. 1 (a) DCT process, (b) Experimental configuration, (c) End mill cutting tool, (d) Top view of the cutting tool showing thrust force (F_{th}), tangential force (F_{tan}), and cutting direction, (e) Schematic display of stand-off distance of nozzle-1 (N-1) and nozzle-2 (N-2) from cutting tool periphery, (f) position of N-1, (g) hybrid cooling/milling environment (HME), and (h) position of N-2

To observe the end milling process of the $Ni_{55.6}Ti_{44.4}$ alloy shape memory alloy in the preliminary stage using the milling setup (shown in

Fig. 1), some pilot trial tuns were sequenced. This pilot experimentation encompassed pre-decided ranges of input variables: cutting-speed (20-80 m/min), feed rate (0.050-0.275 mm/tooth), depth of cut (0.5-3.0 mm) with the cutting tools (in untreated and cryo-treated forms) and cooling environments (WME, HME, and CME). To discover the optimal levels amid these pilot runs, L27 experimental design with four factors (3^{4-1}) fractional factorial model was considered for each cutting tool type. Therefore, while considering both untreated and cryo-treated end mill cutting tools, the experimental design turned into a $2\times3^{4-1}$ mixed fractional factorial design. Also, when considering the L27 array coded in three levels (-1,0,1), the levels of the fourth factor could be achieved as $x_4 = (x_1 + x_2 + x_3) \bmod 3 - 1$. The second-order response models are obtained through ordinary least squares to the individual responses, also considering the significance of the categorical input variables "*cutting tool*" and "*env*", and their interaction. The significance test is performed through the *t*-test of the regression coefficients. The normality of the residuals is tested through the Shapiro-Wilk normality test, while the variance homogeneity is tested through the Breusch-Pagan test. The significance level adopted is $\alpha = 0.05$. The statistical analysis was conducted using R language. The R packages ggplot2, ggpubr, GGally, and olsrr were also used to perform the analysis [26]. After conducting a series of pilot trial tuns, the input variables and their levels, impacting the output variables most effectively, were chosen for the final experimentations, and are shown in Table 1. Each experiment was repeated 3 times and the average values were recorded.

Table 1 Input variables and levels

	Input	unit	Levels		
			-1	0	1
x_1	Cutting-speed (V_c)	m/min	25	40	55
x_2	Feed rate (f_z)	mm/tooth	0.075	0.15	0.225
x_3	Depth of cut (a_p)	mm	1.0	1.5	2.0
x_4	Cutting tool	-	cryo-treated	-	untreated
x_5	Cooling environment (env)	-	WME	HME	CME

2.2 Measuring setup

After milling the samples, the measuring setup aimed to characterize the surface features of the processed parts by measuring the several output variables. Each measurement was conducted three times, followed by their averaging to achieve better accuracy.

For this reason, Precise/TR110 Plus surface roughness (R_a) measuring equipment and Blue Star Ltd./ BSHT-FHV1-50 microhardness (MHD) testing devices were used to measure the produced surface roughness and microhardness of the milled surfaces, respectively. The roughness was analyzed over each machined surface by running the device-probe on a sampling length of 1 mm at three different sites, followed by the calculation of their average. Whereas up to 500 gf load was applied for 15 seconds via a Vickers diamond-tool-indenter at three distinct places on the machined sample, followed by obtaining the average value.

Further, the FESEM and EDS analyses were conducted via FESEM-GeminiSEM 500, Zeiss to analyze the milled surfaces of interest to endorse the results. Additionally, the application of a Rigaku-TTRAX III XRD setup with CuKα radiation (λ: 1.5406 Å), continuous scan speed: 2°/ minute (2Θ range of 20°-120°), and collection of spectra at 0.01° step-size, was included to study the crystalline phases of the machined surfaces of interest. Moreover, the previous studies on the cryogenic machining of Nitinol reported a substantial variation in the phase transformation characteristics of the machined surface and subsurface [41]. Therefore, a DSC (NETZSCH/STA 449 F3 Jupiter) facility was used in the range of 25 ºC to 130 ºC at a rate of 10 ºC/minute to qualitatively determine the milling-induced phase transformation temperature of the surface of interest weighing 94.2815 mg.

In addition, the measurements of the surface energy of the surface of interest were conducted in terms of contact angle (CA), followed by the application of the sessile-drop approach using a Drop Shape Analyzer (DSA10, Krüss). A syringe tip with a suspended droplet of DI-water (1 µL), was guided towards the surface of interest at three different sites until they both experienced substantial contact and subsequently, snaps of the droplet were clicked at 0.4-millisecond time intervals for 60 seconds. A similar temperature and humidity ambiance was used during each test run. Also, since the topography of a surface, for instance, surface roughness [42], can remarkably impact the cell growth and proliferation rates on it, the present study included the analysis of the same for the surface of interest. For this reason, the mean roughness (R_m), root-mean-square roughness (R_q), the maximum peak-to-valley height of roughness (R_t), and mean peak-to-valley height of roughness (R_z) profiles, were measured with the assistance of Alicona-Mex software on Tescan-Vega3 scanning electron microscope (SEM).

Further, to predict the biocompatibility of the finally produced $Ni_{55.6}Ti_{44.4}$ alloy surface, exhibiting the most improved surface roughness and microhardness, cell adhesion and a morphological study were conducted. This examination incorporated commercially pure titanium (CpTi) and the adipose-derived stem cells (ADSCs) for the control and cell adhesion assessment purposes, respectively. CpTi is frequently opted for orthopedic and dental implant applications owing to its remarkable biocompatibility [43]. In addition, ADSCs, which are conveniently obtained from human fat tissue, are extensively adopted for investigating the biocompatibility of numerous biocompatible materials used in orthopedic applications [44]. Dr. Kimberly Cox-York from the Department of Food Science and Human Nutrition, Colorado State University, CO, USA, granted the human ADSCs from adipose tissue (in passage 4) for the present research. The protocol for ADSC segregation from personals with no health issues was approved by the Institutional Review Board of Colorado State University, CO, USA. The first step of this segment of experimentation consisted of the sterilization of CpTi and the obtained $Ni_{55.6}Ti_{44.4}$ alloy's surface of interest with 70 % ethanol and a fifteen-minute incubation. The next step comprised three successive rinses and a thirty-minutes incubation with sterile phosphate-buffered-saline (PBS). The cells were cultured in a suitable growth environment (temperature: 37 °C, CO_2: 5%) comprising α-MEM Media (HyClone™) with 10 % (v/v) Fetal Bovine Serum (FBS, Gibco) and 1% (v/v) penicillin/streptomycin (Corning) [45].

The finally chosen concentration for seeding the sterilized surfaces was 2.0×10^4 cells/mL. The cell adhesion along with the characterization and morphological studies were executed using a fluorescence microscope (Zeiss), nuclear stain 4′,6-diamidino-2-phenylindole (DAPI, 300 nM, Thermo Fisher Scientific), and a scanning electron microscope (JEOL 6500), respectively. The cells were cultured for 4 days on both surfaces, followed by the freeing and a subsequent rising (with PBS) of the surfaces at the end of the 4th day. A fifteen-minute incubation in 3.7 % formaldehyde in PBS was used to fix the cells adhered to both surfaces, followed by three successive rinses (5 minutes each) with PBS. The incubation was then executed with 1% Triton X-100 (Fisher, 98 %) in PBS for 3 minutes, with subsequent twofold rinsing with PBS [43]. The next stage consisted of another five minutes of incubation (with dark surroundings) of both surfaces in nuclear stain DAPI (300 nM, Thermo Fisher Scientific), with successive rinsing and incubation in PBS up to the consequent imaging. The images were captured by employing a fluorescence microscope (Zeiss). In addition, the cleaved ADSCs on the surfaces were ascertained using the ImageJ software by calculating the number of stained nuclei (DAPI). The comprehensive information on the assay and fixation process is easily accessible in the available supplementary materials [46]. At the end of the 4th day, the surfaces were released from the media and rinsed in PBS for the required cell morphological characterization via scanning electron microscopy (SEM). The next step included the positioning of the surfaces in a primary fixative solution composed of 3% glutaraldehyde (Sigma), 0.1 M of sodium cacodylate (ACROS Organics), and 0.1 M sucrose (Fisher) in

DI (deionized) water for 45 minutes. Further, the surfaces were driven into a buffer solution (fixative without glutaraldehyde) for 10 minutes. The later stage consisted of their dehydration by exposing them to ethanol solutions (35%, 50%, 70%, and 100%, respectively) for 10 minutes in each step, and incubation in 100% hexamethyldisilazane (HMDS, Sigma) for 10 minutes. At last, the HMDS was removed with successive drying, and SEM imaging was conducted on the surfaces.

3. Analysis

This section presents a statistical study of the milling experimental runs using WME, HME, and CME and untreated and cryo-treated cutting tools. The latter part of this section demonstrates the morphological study of the milled surface(s) and cutting tool(s) of interest. The following subsections (3.1, 3.2, 3.3, and 3.4) of this section present the obtained findings:

3.1 Statistical analysis

Table 2 presents the L27 experimental design results in terms of average values of R_a and MHD after three repetitions of each trial with the untreated and the cryo-treated cutting tools.

Table 2 L27 experimental design and results

Trial run	Input variables				Output variables			
					Untreated cutting tool		Cryo-treated cutting tool	
	V_c (m/min)	f_z (mm/tooth)	a_p (mm)	env	R_a (µm)	MHD (HV)	R_a (µm)	MHD (HV)
1	25	0.075	1.0	WME	0.64	273.6	0.69	293.8
2	25	0.075	1.5	CME	0.39	314.2	0.81	277.4
3	25	0.075	2.0	HME	0.53	301.7	0.44	324.7
4	25	0.150	1.0	CME	0.49	306.5	0.97	268.9
5	25	0.150	1.5	HME	0.67	291.3	0.58	315.7
6	25	0.150	2.0	WME	0.77	261.4	0.83	284.8
7	25	0.225	1.0	HME	0.75	276.2	0.67	303.5
8	25	0.225	1.5	WME	0.91	248.6	0.89	271.6
9	25	0.225	2.0	CME	0.59	294	1.12	257.4
10	40	0.075	1.0	WME	0.51	288.9	0.53	307.6
11	40	0.075	1.5	CME	0.33	327.3	0.68	291.5
12	40	0.075	2.0	HME	0.45	312.6	0.31	340.3
13	40	0.150	1.0	CME	0.42	315.2	0.82	280.5
14	40	0.150	1.5	HME	0.55	300.3	0.4	329.3
15	40	0.150	2.0	WME	0.66	274.5	0.65	297.3
16	40	0.225	1.0	HME	0.63	285.4	0.51	316.7
17	40	0.225	1.5	WME	0.77	260.6	0.78	284.2
18	40	0.225	2.0	CME	0.51	304.9	0.93	269.8
19	55	0.075	1.0	WME	0.43	302.2	0.4	319.6
20	55	0.075	1.5	CME	0.28	339.5	0.56	302.4
21	55	0.075	2.0	HME	0.36	325.7	0.21	352.8
22	55	0.150	1.0	CME	0.34	327.9	0.7	292.5
23	55	0.150	1.5	HME	0.44	313.2	0.29	341.7
24	55	0.150	2.0	WME	0.52	290.4	0.49	308.3
25	55	0.225	1.0	HME	0.53	298.7	0.38	329.8
26	55	0.225	1.5	WME	0.64	272.4	0.61	295.5
27	55	0.225	2.0	CME	0.45	311.9	0.8	281.2

Table 3 presents the coded response model coefficients of the response R_a considering the numerical input variables in the coded scale and the categorical variables. The model presents intercept, linear, quadratic, and interaction coefficients, besides additive constants to change the milling environment and cutting tool.

Table 3 Response model of R_a

Term	Estimate	Pr(>|t|)	
Intercept	0.8213	<2.00E-16	***
x_1	-0.1197	<2.00E-16	***
x_2	0.1089	<2.00E-16	***
x_3	0.0058	0.292	
$x_1{}^2$	0.0081	0.399	
$x_2{}^2$	-0.0044	0.641	
$x_3{}^2$	-0.0036	0.705	
env HME	-0.4006	<2.00E-16	***
env WME	-0.1689	1.89E-13	***
untreated cutting tool	-0.3989	<2.00E-16	***
$x_1 x_2$	-0.0108	0.113	
$x_1 x_3$	-0.0008	0.901	
$x_2 x_3$	-0.0006	0.953	
env HME: untreated cutting tool	0.5233	<2.00E-16	***
env WME: untreated cutting tool	0.3967	<2.00E-16	***
$R_{adj}{}^2$	0.9725		
Shapiro-wilk	0.8968#		
Breusch-Pagan	0.7271#		

p-values

Signif. codes: 0 ‘***’ 0.001 ‘**’ 0.01 ‘*’ 0.05 ‘.’ 0.1 ‘ ’ 1

The reference milling environment is CME, while the reference cutting tool is cryo-treated. To change the milling environment and/or cutting tool, it is necessary to sum up the related constant.

Further, Fig. 2 shows the mean plot of R_a considering the interaction between the cutting tool and the milling environment, whereas Fig. 3 (a) presents the effects plot considering the numerical input variables and the milling environments for the untreated cutting tool.

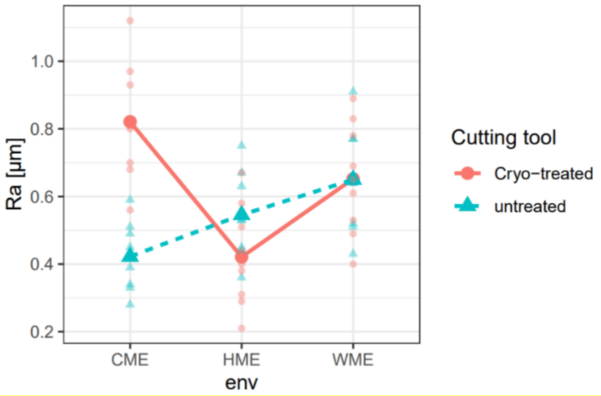

Fig. 2 Mean plot of R_a considering cutting tool and milling environment interactions

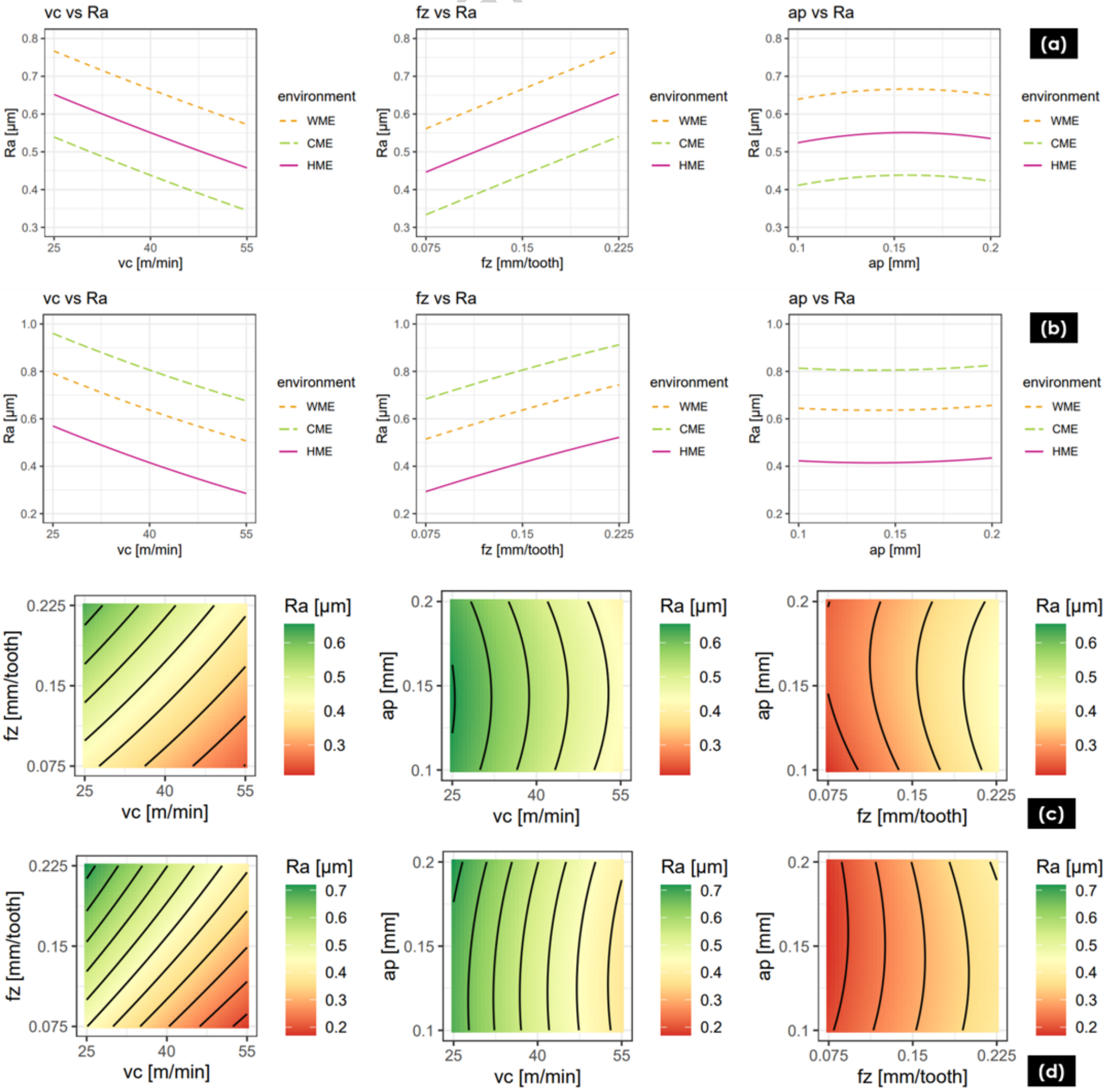

Fig. 3 Effects plot of R_a obtained with (a) untreated and (b) cryo-treated cutting tool; Contour plot of R_a obtained with (c) untreated cutting tool amid CME and (d) cryo-treated cutting tool amid HME

Table 4 demonstrates the response model of MHD and Fig. 4 shows the mean plot of MHD considering the interaction between the cutting tool and the milling environments.

Table 4 Response model of MHD

Term	Estimate	Pr(>|t|)	
Intercept	280.188	<2.00e-16	***
x_1	12.2333	<2.00e-16	***
x_2	-12.039	<2.00e-16	***
x_3	0.17222	0.5198	
x_1^2	-0.0778	0.8664	
x_2^2	-1.1444	0.0171	*
x_3^2	0.7722	0.1007	
env HME	48.9694	<2.00e-16	***
env WME	15.6778	<2.00e-16	***
untreated cutting tool	35.5333	<2.00e-16	***
$x_1 x_2$	-0.775	0.0220	*
$x_1 x_3$	-0.0792	0.8087	
$x_2 x_3$	0.86944	0.0658	.
env HME: untreated cutting tool	-63.244	<2.00e-16	***
env WME: untreated cutting tool	-56.656	<2.00e-16	***
R_{adj}^2	0.9955		
Shapiro-wilk	0.6332#		
Breusch-Pagan	0.8096#		

p-values

Signif. codes: 0 '***' 0.001 '**' 0.01 '*' 0.05 '.' 0.1 ' ' 1

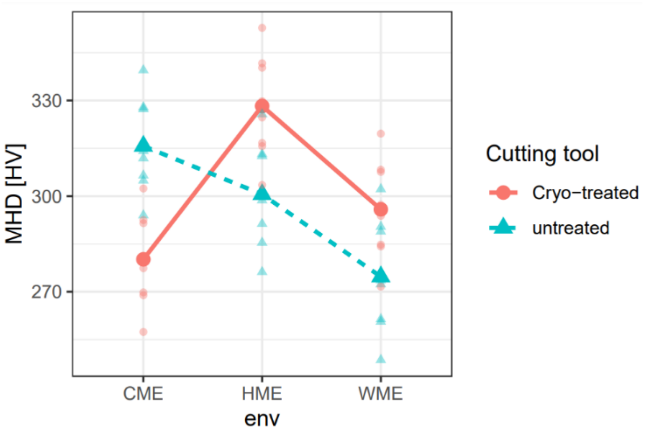

Fig. 4 Mean plot of MHD considering cutting tool and milling environment interactions

In WME, the cryo-treated cutting tool showed better results. In general, improved results were achieved with the cryo-treated cutting tool during HME. Taking into consideration the best combination of cutting tool and milling environment to achieve the highest microhardness results, Fig. 5 (a) and (b) show the effects plots of MHD varying the numerical input variables with the untreated and cryo-treated cutting tool, respectively. Fig. 5 (c) and (d) show the contour plots of MHD with the untreated and cryo-treated cutting tools, respectively.

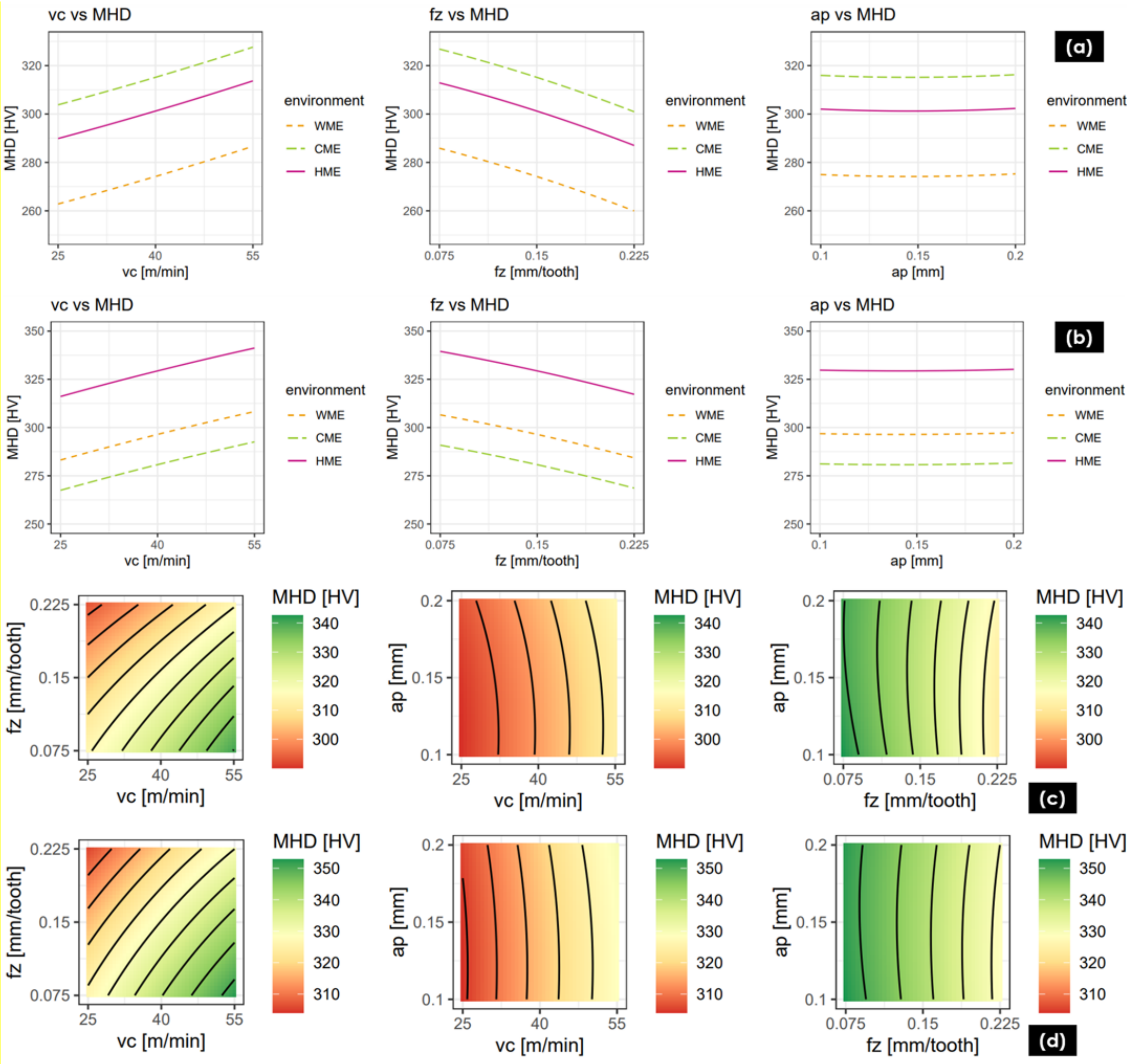

Fig. 5 Effects plot of MHD obtained with (a) untreated and (b) cryo-treated cutting tool; Contour plot of MHD obtained with (c) untreated cutting tool amid CME and (d) cryo-treated cutting tool amid HME

Fig. 6 shows the pairs plot of R_a and MHD considering the milling environment and cutting tool in the color scale. The First column of plots shows color identification of the milling environment and the scatter of the two responses. In general, HME presented the highest MHD and smallest roughness, followed by CME, and WME. The second column plots R_a on a horizontal scale, and the cooling environment on colored scale. The point distribution is shown in the bottom with the bottom box considering the untreated tool, and the upper box with the cryo-treated tool.

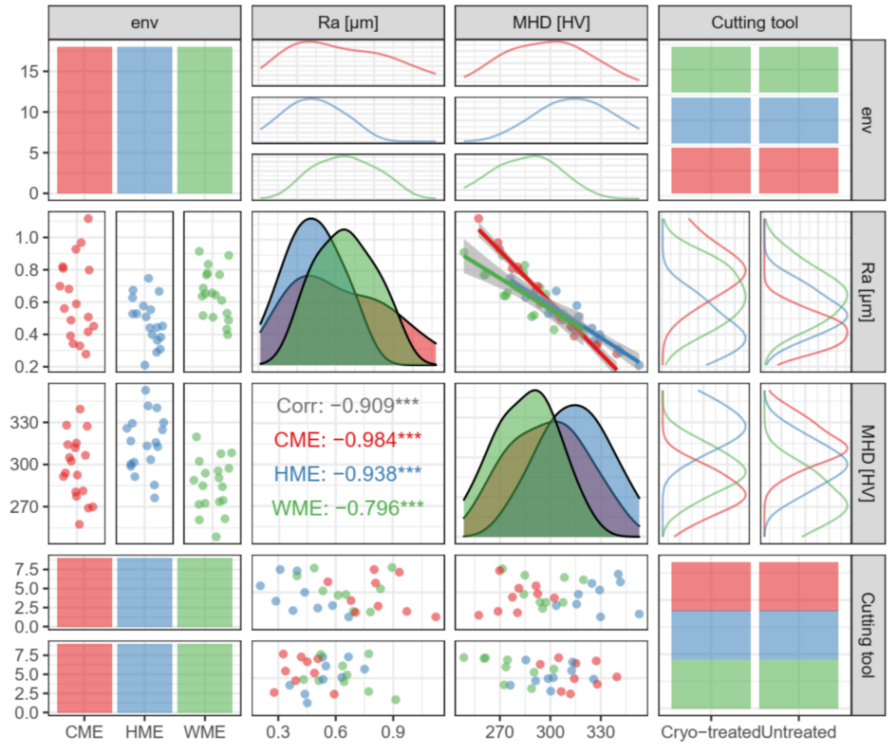

Fig. 6 Pairs plot

3.2 Characterization of the surface milled by cryo-treated cutting tool

In accordance with two previous studies [21, 47], the major cause of considerable improvement in surface roughness and microhardness amid CME and HME is hypothesized to be the temperature of the cooling environment which is low enough not only to refine the grains but also to induce strain hardening and thus, dampen the cutting temperature and thermal softening, via rapid cooling. However, WME, with a cooling environment of relatively high temperature, might have caused increased regional softening, resulting in thermal smearing, and thus, poor surface quality. In this regard, Fig. 7 presents the FESEM images of the top and front views (at different magnifications) of the two surfaces produced by the cryo-treated cutting tool during HME (Fig. 7 (a), (b), and (c)) and CME (Fig. 7 (d), (e), and (f)), respectively.

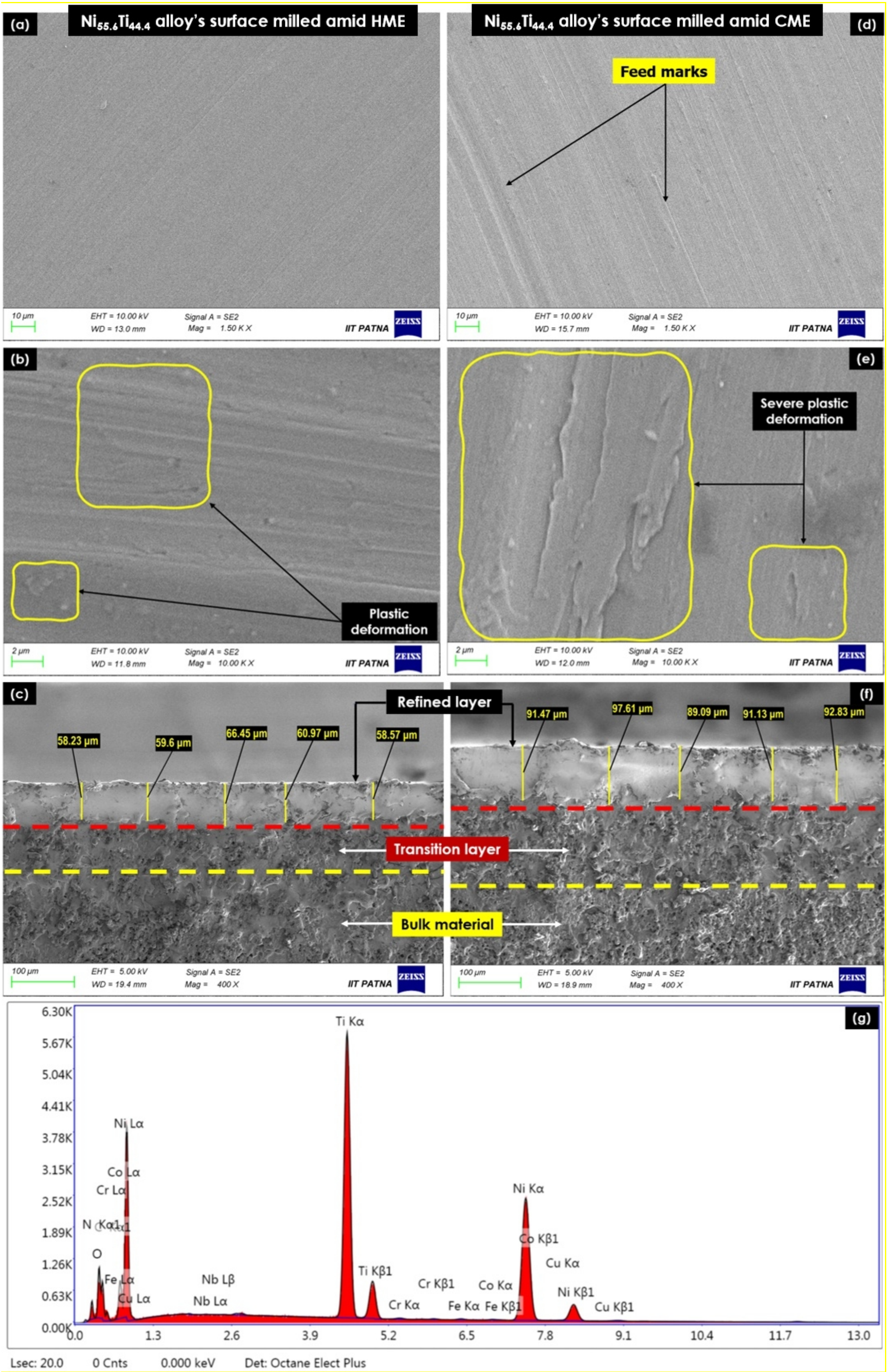

Fig. 7 (a) and (d) Top view at 1.50 K×, (b) and (e) top view at 10 K ×, and (c) and (f) front view at 400 × of the surfaces produced by cryo-

treated cutting tool amid HME and CME, respectively; (g) EDS plot of the surface produced amid HME

Additionally, the literature also records a noticeable effect of the cutting-speed on the phase transformation of Nitinol [41]. Therefore, the HME-milled $Ni_{55.6}Ti_{44.4}$ alloy surface of interest was further analyzed by XRD for a basic crystalline phase determination with the help of the peak appearances, indicating the phases present. The X-ray diffractogram of the HME-milled surface is displayed in Fig 8.

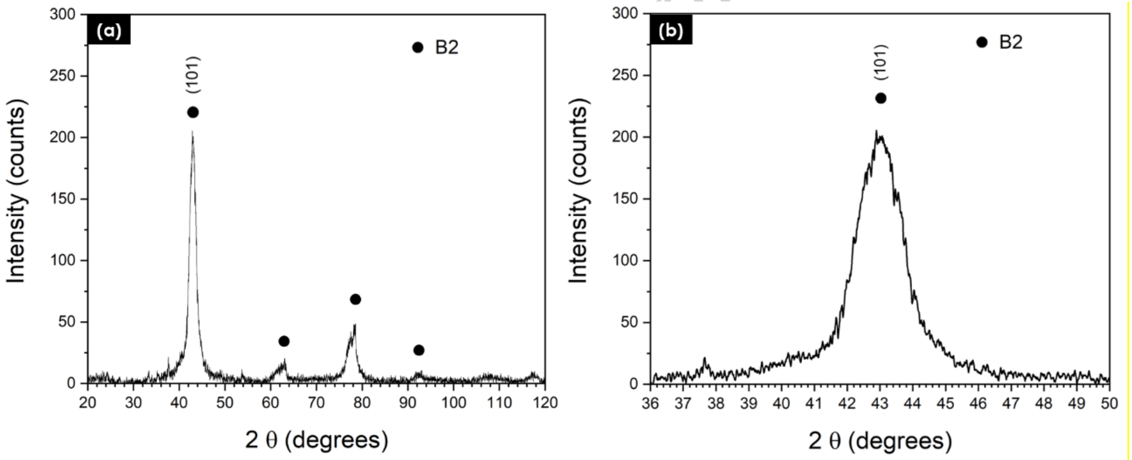

Fig. 8 XRD diffractogram of the HME-milled $Ni_{55.6}Ti_{44.4}$ alloy surface

Besides, to qualitatively ensure the phase transformation characteristics at the HME-milled surface, the DSC response of the same was obtained and is displayed in Fig. 9.

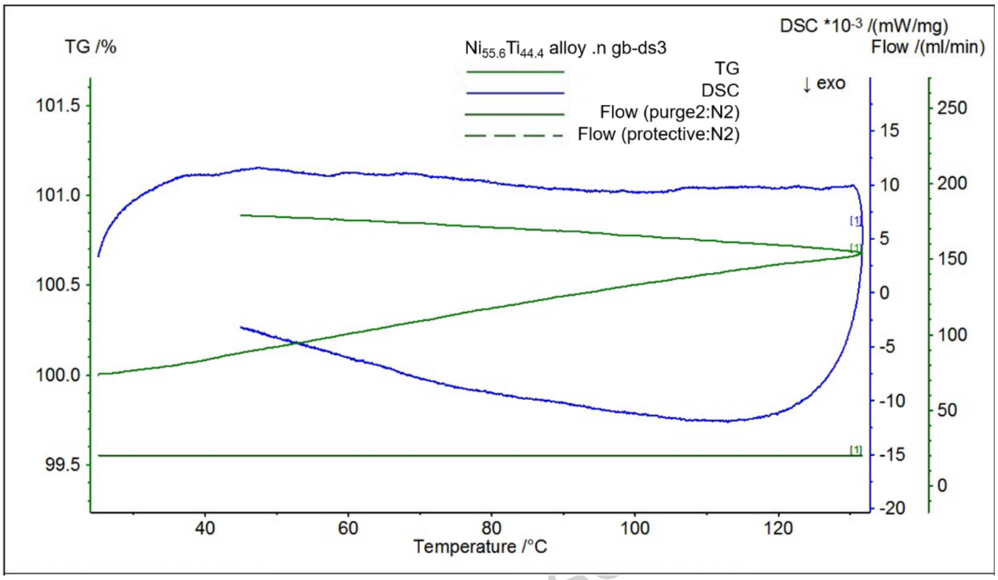

Fig. 9 DSC response of the HME-milled $Ni_{55.6}Ti_{44.4}$ alloy surface

3.3 Investigation of the bioactivity of HME-milled surface

This section includes a brief study to examine the possible bioactivity of the modified $Ni_{55.6}Ti_{44.4}$ alloy surface. For this reason, the wetting, topographic, and biocompatibility characteristics of the modified $Ni_{55.6}Ti_{44.4}$ alloy surface were further investigated.

The enhancement in wettability of the modified $Ni_{55.6}Ti_{44.4}$ alloy surface is displayed in Fig. 10 (a). The circle-fitting profile was used for getting the CA values to fit. The CA measurements were observed with an average value of 92 ° as soon as the pre-determined time of 60 seconds was over. On the other hand, the three-dimensional images showing the roughness measurements can be seen in Fig. 10 (b).

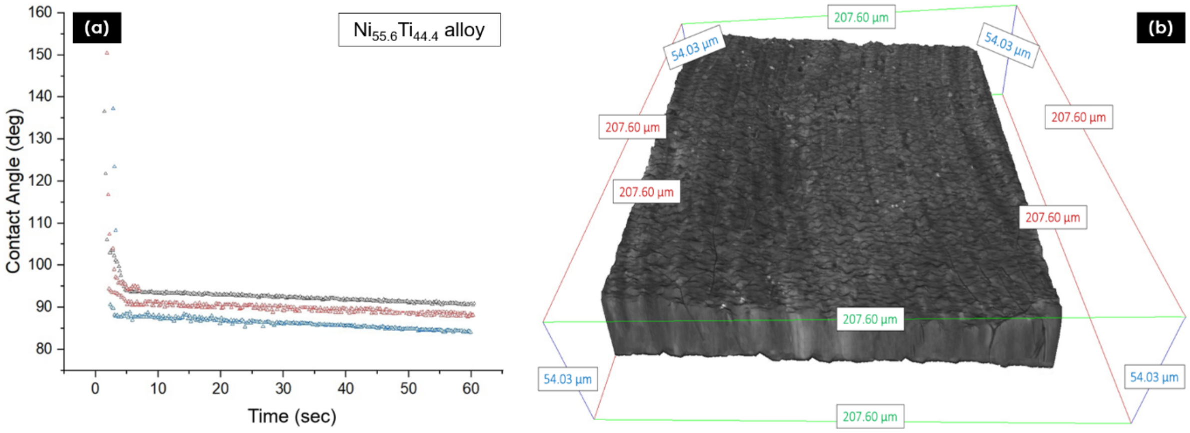

Fig. 10 (a) Static water CAs with respect to time and (b) three-dimensional recreated view for modified $Ni_{55.6}Ti_{44.4}$ alloy surface

Additionally, the biological properties of the modified $Ni_{55.6}Ti_{44.4}$ alloy surface were validated by a short-term biocompatibility study. Cell adhesion and morphology were investigated on CpTi and the $Ni_{55.6}Ti_{44.4}$ alloy surface produced by the cryo-treated cutting tool during HME. Since osteogenic differentiation gets considerably influenced by the initial stem cell adhesion, the functional performance of the implant is also affected [46]. Hence, the present study focused on the $Ni_{55.6}Ti_{44.4}$ alloy's capability to promote the adhesion and spread of ADSCs by presenting the fluorescence, SEM, and graphical images via Fig. 11 (a), 11 (b), and 11 (c), respectively.

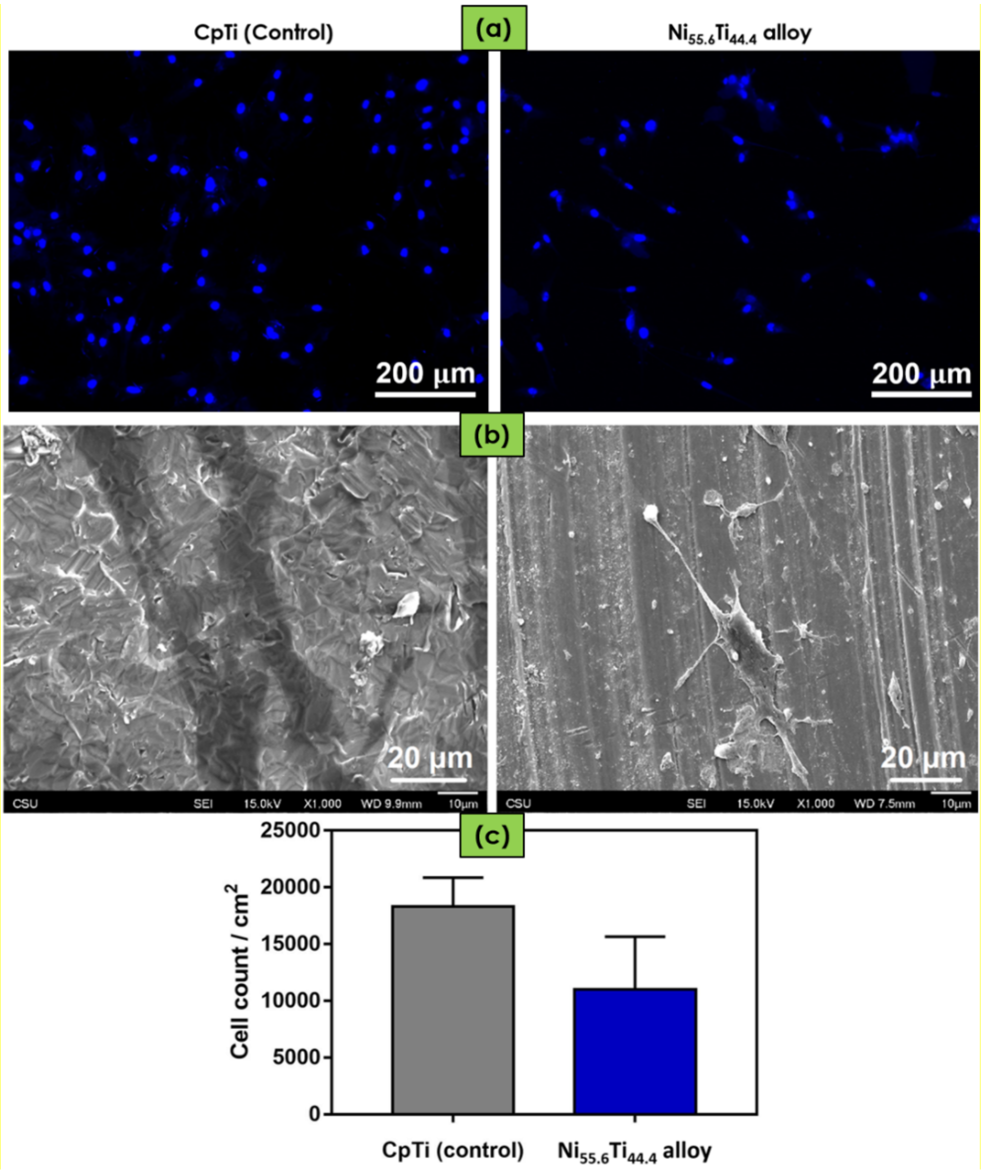

Fig. 11 (a) Fluorescence microscopic images demonstrating ADSCs stained with DAPI (blue) after 4 days of cell culture on both surfaces, (b) SEM images (at 1000× magnification) of ADSCs on both surfaces after 4 days of cell culture, and (c) Cell count per area after 4 days of ADSCs culture. No noticeable distinction in cell count could be noted between the surfaces. The outcomes were statistically analyzed using the Tukey test at a 5% significance level

3.4 Morphological study of the cryo-treated cutting tool

In this work, since the untreated end mill cutting tools encountered relatively more wear than the cryo-treated ones, a total of three cutting tools were successfully used in untreated conditions and two in cryo-treated conditions to finish all the experimental trials. The cryogenic treatment of carbide cutting tools generally enlarges the particle size and refines the grain structure, thus, improving their thermal conductivity. Consequently, an intensified heat dissipation is reported, which must be the plausible reason for the better functioning of the cryo-treated cutting tool than the untreated one [26]. Also, both the low temperature cooling approaches (HME and CME) profoundly reduced the cutting tool wear and thus minimized the geometrical alteration of the workpiece. Therefore, this section of this paper focuses only on the morphological study of cryo-treated cutting tools used amid HME and CME.

The cutting tool generally experiences high heat while processing titanium alloys due to their low thermal conductivity, very high hardness, and strength [26, 48]. Moreover, the end mill cutting tool often encounters severe thermal shock and dynamic heat flux in every rotation. The notable alterations at the cutting edge temperature act in close association with the rapid heating and cooling of the same. Also, the heat transfer is not smooth via work-specimen and chip amid chip-formation, leading to an increase in the total amount of heat faced by the cutting tool [49]. As reported by a research, about 10% of the overall heat produced is experienced by the cutting tool [50]. Consequently, when compared with HME, in the case of CME, the cryo-treated cutting tool must have experienced temperature fluctuations of higher magnitude, leading to developing greater thermal stresses, incurring inevitable cracking (normal to the cutting edge), followed by wear. In addition, in a milling process, the temperature change that reduces the hardness [51] and induces thermal cracking, might be aggravated mainly in the presence of water-based conventional fluids [49] and cryogenic cooling [26] as well. Hence, based on these facts, both the cutting tools noted with striking wear, are shown in Fig. 12.

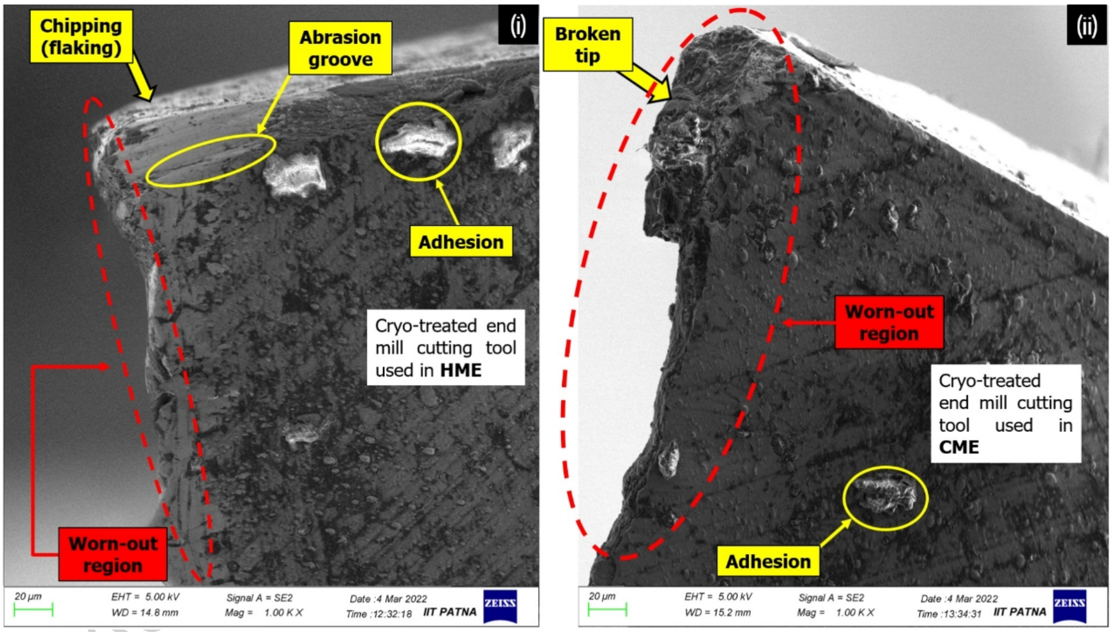

Fig. 12 FESEM images (1000 ×) showing the worn-out and damaged regions (by breakage) on the cutting edges of the cryo-treated cutting tool used in (i) HME and (ii) CME at the optimized setting of input variables

4. Discussion

This section further discusses the results observed in the previous subsections 3.1, 3.2, 3.3, and 3.4 of section 3 in the following subsections 4.1, 4.2, 4.3, and 4.4, respectively:

4.1 Statistical response

In Tables 2 and 3, it can be observed that there is a significant statistical difference between the milling environments and cutting tools, besides the interaction between both. The linear effect of V_c and f_z (x_1 and x_2) are statistically significant. There is no quadratic or interaction effect of the numerical input variables. The R_a model presents good data variability accounting, with 0.9725 of explained proportion. The assumptions of normality of the residuals and homoscedasticity of the response cannot be rejected, considering the Shapiro-Wilk normality test of the residual and the Breusch-Pagan test, respectively. In the wet milling environment, both cutting tools presented similar results. Both CME and HME were reported to exhibit lower surface roughness values compared to WME, possibly due to the controlled plucking and smearing action as a result of lower temperature cooling environments [52].

Further, it is evident in Fig. 2 that with CME, the untreated cutting tool obtained the lowest roughness, whereas, with HME, the cryo-treated cutting tool produced the lowest roughness. Possibly, the thermal properties of the CME did affect the surface roughness of the workpiece while being processed with the untreated cutting tool. Also, the moderate temperature of HME credibly cooperated well with the enhanced characteristics of the cryo-treated cutting tool. These observations might be supported by some recent studies where the optimal cutting temperature aided in maintaining the cutting tool’s hardness, minimizing the chances of shape deterioration and thus reducing surface roughness [53]. Also, the controlled temperature in the milling zone (as a result of CME and HME), could credibly decrease the thermal and mechanical loading, leading to the development of less deformation region, and thus enhanced surface quality [9]. Further, in Fig. 3 (a), it is indisputable that cutting-speed presents a negative effect on roughness, while the feed rate shows a positive effect on the same. Confirming the significance of the test presented in Table 3, the cutting depth effect can be neglected. These observations confirm CME as the best milling environment when milling using the untreated cutting tool. Additionally, Fig. 3 (b) presents the effects plot considering the numerical input variables and the milling environments for the cryo-treated cutting tool. The effects of the numerical input control variables are similar to the ones detected with the untreated cutting tool. However, the cryo-treated cutting tool performs the best amid HME. As the feed rate rises, the roughness is expected to increase due to the geometrical periodic effect and some uncut surfaces during the material removal process. However, the rise in the cutting-speed can result in the reduction of friction and temperature due to the increase in material subtraction, entailing in the increase of roughness. The presented model of R_a depicted in Table 3 can be selected according to the milling environment and cutting tool type, and further, the best ones can be selected. Fig. 3 (c) shows the contour plot of R_a when selected the untreated cutting tool and CME. Fig. 3 (d) shows the contour plot of R_a when selected the cryo-treated cutting tool and HME. The discussed influence of the numerical input variables may be confirmed as the lowest roughness levels were achieved with the highest cutting-speed and lowest feed rate, for both considered combinations of cutting tool-milling conditions. The low levels of feed rate and depth of cut and high level of cutting-speed in association with cryogenic treatment of cutting tools, often lead to the improved performance of cryo-treated cutting tools even at high machining-temperatures, resulting in enhanced surface finish [54]. Moreover, the contending lubricating properties of CME and HME, in the case of untreated and cryo-treated cutting tools, were another possible reason that could notably protect the cutting tool against friction and abrasion, enhancing the surface quality [53]. However, the higher levels of feed rate and cutting depth demand a higher amount of power and cutting forces, which possibly resulted in higher surface roughness. Therefore, the obtained findings are found in compliance with one of the previous studies [26].

Besides this, as per the observations noticed in Table 4, the same input variables and levels that were significant in the case of R_a were found significant in the case of MHD too, however, with the changed sign. When roughness increases it is expected that the microhardness decreases, as a rough surface will have less resistance to the indenter penetration. The linear effect of V_c and f_z (x_1 and x_2) are statistically significant. The quadratic effect of feed rate is also statistically significant. The MHD model presents good data variability accounting, with 0.9955 of explained proportion. The assumptions of normality of the residuals and homoscedasticity of the response cannot be rejected, considering the Shapiro-Wilk normality test of the residual and the Breusch-Pagan test, respectively.

Further, it can be noticed in Fig. 4 that with CME, the untreated cutting tool achieved the highest microhardness, while with HME, the cryo-treated cutting tool attained the highest microhardness. The optimal cooling temperatures amid CME and HME, while working with the untreated and cryo-treated cutting tools, respectively, possibly prevented the decimation of plastic deformation, leading to improved microhardness [55]. Another possible explanation for the increase in the same is improved twinning in the Nitinol workpiece's microstructure (after successful machining) that raises the grain boundaries [56]. The CME and HME-induced cooling effects could possibly regulate the subsurface thickness (by limiting the plastic deformation), and could thus diminish the development of twinned martensite, resulting in enhanced microhardness [30].

The statistical tests performed and summarized in Tables 3 and 4 primarily focus on the effects of the cooling environment and cutting tool type. In Fig. 2 and 4, the clusters of points distributed around each average point are the experimental observations. However, the average points in the plots only reflect the change regarding the effects of the environment and cutting tool. For each one of the 6 combinations of tool and environment, there are 9 observations that represent distinct combinations of V_c, f_z, and a_p. Therefore, the spread among these points is natural due to the change in cutting conditions. It is necessary to understand that irrespective of the variation in input variables, the analysis in Tables 2 and 4 assures that the studied effects of the cooling environment and cutting tool are statistically significant, which means that higher than the experimental error.

Additionally, in Fig. 5 (a) and (b), the cutting-speed presents a positive effect on microhardness, while the feed rate presents a negative effect on microhardness. Cryo-treated cutting tool during HME induced the highest microhardness. In Fig. 5 (c) and (d), the discussed effect of cutting-speed and feed rate are confirmed, and the highest microhardness is attained with the lowest feed and highest cutting-speed levels. The cryo-treated cutting tool attained higher R_a and lower MHD possibly due to an additional increase in its hardness and reduction in cobalt binder β-phase when used during CME (-196 °C), resulting in the rise in brittleness [27]. Thus, during the interaction with the CME-induced hardened surface, the brittle cryo-treated cutting tool would be prone to disintegrate carbides, followed by severe wear or breakage due to a large amount of cutting effort and consequently deteriorate the surface quality. Hence, the damaged cryo-treated cutting tool is expected to rub against the surface, leaving feed marks behind and obtaining higher R_a. This finding is in agreement with a recent study [25]. Further, among all the input variables, although the rise in feed rate had a negative effect on the output variables, it was adequately regulated amid HME with both untreated and cryo-treated cutting tools, displaying the potential cooling, and lubricating action of HME. LN_2 does not seem to alter the existing characteristics of the cutting fluid, but it did improve the overall cooling and lubrication when used together with the milling process. This outcome could be supported by a previous study, where a significant reduction in the resistance between the tool and chip interface was hypothesized as an outcome of the improved cooling and lubricating action of hybrid cooling, leading to plough the surface with a force of higher in magnitude than the cutting force [21]. Further, in comparison to CME, HME exhibited a better lubrication effect, which could be explained in terms of the axial depth of cut, used in the present study. While considering the axial depth of cut, the end mill helix is more susceptible to the adherence of removed chips followed by catastrophic failure, the produced surface would possibly be subjected to higher cutting forces and thermal loading [26]. Hence, the enhanced surface characteristics of the HME-milled surface once again confirm its superior performance. Generally, milling with high cutting-speed, low feed rate, and depth of cut considerably reduce the energy required for the chip-formation (plastic deformation) and thus heat and mechanical loading. Consequently, the subsurface layer’s thickness also gets decreases and hence possesses a relatively less number of twinned martensite structures (oriented in distinct directions) [53]. In Fig. 5, the cutting-speed was noticed with a positive linear effect on roughness, while the feed rate presented a negative linear effect on the same, with statistical significance. The effects of cutting tool and milling environment levels were also found to be statistically significant. In addition, reduced feed rate and depth of cut enable the formation of thinner chips and thus facilitate their easy removal, resulting in the decreased magnitude of the cutting force. Also, the deformation hardening might have occurred in the Nitinol workpiece, since its austenite phase possibly changed to a martensite phase due to the notable cooling effects of CME and HME, leading to a considerable increase in the microhardness [55].

Apart from this, it could be observed in Fig. 6 that for the untreated tool, the distribution of points confirms CME as the best one to achieve the lowest roughness, followed by HME, and WME. For the Cryo-treated tool, the best roughness results are achieved with HME, followed by, WME, and CME. Following, the points plot for Ra, in the second column, it is presented the Person correlation coefficient between the two outputs. The general correlation presented in grey is negative and higher (-1 would be a perfect negative correlation), which means that microhardness decreases with the increase of roughness. Harder surfaces present high resistance to superficial integrity changes. The negative correlation is also significant when observed in each environment, with more prominence in CME, followed by HME, and WME. Above the correlation coefficients it is shown density plots first overlaid, and above all separated in distinct panels by the environment. As can be observed, HME presented asymmetric distribution with the highest probability in smallest roughness values, CME also presented asymmetric distribution with the highest probability in smallest roughness values but not so accentuated as HME, and WME presented a symmetric distribution, with the highest probability in intermediate roughness results. The third column presents MHD on a horizontal scale. At the bottom point plots are presented. For the untreated tool, the distribution of points confirms CME as the best one to achieve the highest MHD, followed by HME, and WME. For the Cryo-treated tool, the best MHD results are achieved with HME, followed by, WME, and CME. Above it is presented the overlaid density plots. HME presented asymmetric distribution with the highest probability in the highest MHD results, CME presented symmetric distribution with the highest probability in intermediate MHD results, and WME presented asymmetric distribution with the highest probability in small MHD results. Above overlaid density plots it is presented scatter plots with regression lines considering each environment. The significant negative correlation between MHD and roughness is confirmed. Above scatter plots the density plots for MHD are depicted considering each environment individually.

The last column shows density plot panels considering combinations of environment and Cutting tool type. At the left column, it is plotted the results for the Cryo-treated tool. It is confirmed that HME presented the lowest roughness and highest MHD, followed by WME, and CME when using the Cryo-treated tool. When considering the untreated tool CME presented the lowest roughness and highest MHD, followed by HME, and CME. Generally, the metals being machined are susceptible to getting plastically deformed as a result of work-hardening of the surface. However, the cooling environment determines the volume of this plastic deformation. In the case of highly elastic $Ni_{55.6}Ti_{44.4}$ alloy, its excessive sensitivity towards machining-induced thermal stresses, large strain rate, and ensued phase transformations are some of the main issues complicating its traditional machining. This further adversely affects the cutting tool by increasing tool wear, formed built-up-edge (BUE), chip adhesion, and minor chip breakage. The consequent detrimental effects of the same are often witnessed on the cut surface as grain deformation, tearing, cracks, lay patterns, feed-marks, and slip-zones [57]. Also, since the workpiece surface would experience a notable rise in hardness with the decrease in the machining environment 's temperature (during HME and CME), a greater cutting force would need to be exerted by the cutting tool, leading to more damage to the workpiece surface. Further, when considering the data selected by each milling environment type, the correlation between the two responses remains high. The fourth column shows the box plots considering the two cutting tool types and three milling environments, for both responses. For each response, the three boxplots on the left are with the cryo-treated cutting tool, while the three on the right are with the untreated cutting tool. It is evident that with the cryo-treated cutting tool, the lowest roughness and highest microhardness are achieved during HME, while using the untreated cutting tool, CME ensures the lowest roughness and highest microhardness. The general mechanism of LN_2 dissociating the cutting tool from the chip involves a gas or fluid cushion effect, simultaneous lubricating action, and LN_2's low viscosity and non-adhering properties. The LN_2-assisted lubrication forms steady films that decrease the feed and frictional forces, and the thickness of the secondary deformed layer (within the chip microstructure) [26]. Thus, CME must have induced the highest hardness (causing the least adherence) to the $Ni_{55.6}Ti_{44.4}$ alloy surface due to its lowest temperature by dominating its thermal softening. Whereas HME possibly achieved a hardness value lying somewhere between CME and WME (lower than CME and higher than WME), due to the presence of both cutting fluid and LN_2. Similarly, the $Ni_{55.6}Ti_{44.4}$ alloy surface credibly experienced an adherence that was lesser than WME and higher than CME. The models of R_a and MHD presented in Tables 3 and 4, respectively, are initially based on CME and cryo-treated cutting tools. To change the cutting tool and milling environment, it is necessary to add the related constants. The two best combinations of the categorical input variables are the untreated cutting tool with CME and the cryo-treated cutting tool with HME. Using a cryo-treated cutting tool, when changing the milling environment from CME to HME, it achieves a decrease of 0.406 µm in R_a and an increase of 48.97 HV in MHD. When changing the cutting tool from cryo-treated to untreated under CME, a decrease of 0.398 µm in R_a and an increase of 35.53 HV in MHD, were noticed. Therefore, comparing these two cutting tools and milling environment combinations, the cryo-treated cutting tool and HME presented the best performance in the end milling of $Ni_{55.6}Ti_{44.4}$ alloy.

4.2 Cryo-treated cutting tool-induced surface characteristics

As noticed in Fig. 7 (a) and (d) at 1.50 K× magnification, the surface produced during HME appears to have very nominal feed marks in comparison to the surface produced during CME. However, the presence of visible feed marks on the CME-milled surface is a sign of the cryo-treated cutting tool's weaker performance as a result of considerable wear and damage. On the other hand, HME could substantially decrease the cutting temperatures, and thus, saved the end mill cutting edge from quicker melting and wearing, which further helped in retaining a better cutting tool's geometry resulting in reduced feed marks. Additionally, both surfaces were observed with no thermal cracking, which possibly validates the favorable effect of a low-temperature cooling environment on the machined surfaces. As displayed in Fig. 7 (b) and (e) at 10 K × magnification, the milling-induced plastically deformed surfaces were observed on both the HME and CME-milled surfaces, respectively. Additionally, the HME and CME-induced plastically deformed layers with varying depths are also evident in Fig. 7 (c) and (f) at 400 × magnification. The deeper depth of the CME-induced layer compared to the HME-induced layer points towards the severe plastic deformation on the surface and sub-surface milled under the lowest temperature (-196 ºC). In contrast, the

HME-induced layer appeared to have a lesser depth compared to the CME-induced layer, possibly due to the phase transformation (austenite vs martensite) during distinct cooling environments of milling, and also as a result of a comparatively warm cutting temperature, which could recover a considerable amount of plastically deformed zone. Additionally, the CME can cause the deformation in $Ni_{55.6}Ti_{44.4}$ alloy in the martensite phase (due to the extremely low temperature of LN_2), leading to a fairly high density of deformation twins, and therefore, this might be the credible reason why the plastic deformation was noticed with a deeper layer depth than the HME-induced layer [56]. However, a review article outlined the supportive influence of this plastically deformed layer, consisting of nano-crystalline and work-hardened surfaces, on the fatigue and wear resistance of the machined specimen. According to the Hall-Petch relationship and Zenner-Holloman equations, the low temperature of the cutting environment can substantially regulate the surface deformation by effective refinement of grains and the consequent yield strength. Therefore, the improved subsurface microhardness values (shown in Table 2) noticed in the case of CME and HME, are possibly the result of smaller grains due to the high density of twins [41]. Also, as observed by another study, the surface finish in martensitic phase machining is often inferior to the austenitic phase one, and hence, the relatively poor surface quality observed on CME-milled surface (possibly due to martensitic phase) in the present research falls in agreement with this study [58]. Moreover, based on a previous study, the plastically deformed or affected layer could be further divided into a refined and transition layer and could be identified and located in Fig. 7

(c) and (f). These layers possess different thicknesses, appearances, and mechanical and thermal properties, as a result of various process input variables such as feed rate, cooling medium, speed, cutting tool geometry, and depth of cut [59], nonetheless, the meticulous study of the same does not fall in the current scope of this research. However, the HME-induced layer was preferred due to its lesser thickness (noticed by visual inspection) and better uniformity compared to the CME-induced layer, and hence, was further analyzed with the assistance of EDS examination. Although the HME-milled surface characteristics are substantially different from the CME-milled surface, some of their features might be closely connected or common since HME also contains approximately 50 % LN_2, however, the same will need to be validated in the extended detailed studies. The EDS plot (Fig. 7 (g)) exposes the existence of various elements on the HME-milled surface. The considerable oxide content might induce a nickel-free protective film on this milled surface and might thus, substantially enhance the corrosion resistance and biocompatibility of the same [60]. Besides, the presence of the oxide in the recast layer is attributed to a strong barricade, substantially restraining the corrosion and discharge of harmful Ni ions into the blood flow [61]. The oxide layer formed on the machined surface can substantially delay corrosion in the existence of a corrosive environment by retarding and obstructing the electron migration for electrochemical reactions. Hence, this $Ni_{55.6}Ti_{44.4}$ alloy's implant surface might substantially regulate the metallic ion movement to the human body, and might thus augment the cytotoxicity and resistance to the resultant inflammations [62]. Moreover, a study reported that in comparison to an untreated cutting tool, a cryo-treated cutting tool can induce better uniformity and thickness to the oxide layer [24]. Additionally, the sharp peak of titanium content might point towards the increase in its amount on the milled surface as a result of degraded titanium from the cutting tool surface during its wear. The present research has already discussed a considerably positive influence of high cutting-speed on surface roughness and microhardness in previous sections.

Further, Fig 8 (b) exhibits the bigger view of the higher peak appearing in Fig. 8 (a). In both the views of Fig. 8, the presence of parent-ordered cubic (B2) austenite crystal structures is evident. The only diffraction that appeared is reflecting the austenitic phase and is observed by the (101) plane at 42° (2ϴ). Some of the main reasons for observing the phase transformation in $Ni_{55.6}Ti_{44.4}$ alloy is its comparatively low phase transformation temperature. The induced stresses and excessive generated heat amid a machining process notably tailor the workpiece’s active phase, resulting in a noteworthy variation in the mechanical and thermal properties of the machined surface [30]. Therefore, $Ni_{55.6}Ti_{44.4}$ alloy might be subjected to a stress/low temperature-induced martensite phase or can remain or be restored in the austenite phase, depending on the temperature of the cooling environment and generated heat amid machining [16]. The cooling environments used during machining, having temperature values below the M_f temperature of the $Ni_{55.6}Ti_{44.4}$ alloy specimen, tend to deform the specimen in its martensitic phase during the machining process. However, the B2 austenite phase detected by the XRD is probably the reverse-transformed phase from the deformed martensite phase as a result of heating back to room temperature (26 ºC) as soon as the particular milling operation run got over. A temperature higher than the A_f (10-15 ºC) can easily induce the transformation of deformed martensite into austenite, which is responsible for the disappearance of the martensite phase from the XRD diffractogram [56]. Also, the appearance of only austenite displays an agreement with a few previous studies that did not necessarily observe the martensite peaks on each type of machined Nitinol samples such as dry, preheated, MQL, and cryo-machined, but did witness the distinctive austenite peaks in each case [16, 30, 31]. Moreover, a common challenge faced in the phase identification of low-temperature machined Nitinol samples is the peak-broadening, which is also evident in both Fig. 8 (a) and (b) where only a few narrow and long peaks could be observed [31]. However, a subsequent detailed study will be required in the future to investigate the effect of HME on the phase transformation of $Ni_{55.6}Ti_{44.4}$ alloy.

Besides, as depicted in Fig. 9, the latent heat of transformation for this surface could not be accurately measured in any of the heating or cooling processes due to the unique trend of the obtained plot. Moreover, no noticeable phase transformation was observed in the DSC thermogram with the applied temperature range. The possible reason for the DSC response showing only one phase with no alteration, in the presence of the reverse-transformed austenite phase, was also noticed by the XRD diffractogram. Hence, the indication of no phase transformation or the absence of the martensite phase in the DSC thermogram confirms the finding depicted in the XRD plot (Fig. 8). Also, the consistency in the DSC response implies that the deformation present in the HME-milling-induced layer could substantially decelerate martensite transformation in that zone. The crystal structure of this surface credibly had a high density of vacancies and dislocations, resulting in the suppression of the volume of material subjected to transformation. A somehow similar trend was noticed by some previous research also, however, those were the cases of severe plastic deformation where the cooling curve almost hid the martensitic transformation [56, 63]. Additionally, the modified $Ni_{55.6}Ti_{44.4}$ alloy surface was detected with a 17.44 % higher microhardness value (276 HV) compared to the as-received $Ni_{55.6}Ti_{44.4}$ alloy surface. Hence, all the improvements observed in the HME-milled $Ni_{55.6}Ti_{44.4}$ alloy surface characteristics via FESEM, EDS, and XRD can be interpreted as a substantial modification.

4.3 Bioactivity of HME-milled surface

In continuation of this study, as shown in Fig. 10 (a), the revealed results of wettability ascertained a noticeable hydrophobicity of the modified $Ni_{55.6}Ti_{44.4}$ alloy surface (> 90 ° CA), indicating its considerable affinity towards the blood (as a result of decreased adherence and stimulation of platelets) and controlled potentiality to liberate a drug at the intended site [64]. A rise in wettability is generally noticed with an increase in the formation of hydrogen bonds due to the reaction of hydroxyls with water molecules [65]. Hence, the credible reasons for the observed hydrophobicity are the favorable characteristics of the topmost surface layer (modified layer), such as adequate types and number of chemical compounds, metallurgical properties, and geometrical features including thickness. This finding might be compared with a recent investigation reporting an improved hydrophobicity on an EDMed Nitinol surface [66], suggesting a competent efficiency of the present traditional subtractive manufacturing process when employing the combination of cryo-treated cutting tool and HME. Further, in the presence of an inferior quality surface finish, the Ni element may get released from the Nitinol surface into the blood, forming harmful compounds (toxic) and disrupting the evenness of protective oxide content in the topmost surface layer. In this relation, as shown in Fig. 10 (b), the present study noticed the average numerical value of surface roughness R_m = 341.69 nm, with R_q = 398.22 nm, R_t = 3.02 µm, and R_z = 2.14 µm on the modified $Ni_{55.6}Ti_{44.4}$ alloy surface, suggesting its use in cardiac stent application as surface modifications of the order of nanoscale are preferred to regulate the cellular movements [42]. Hence, this surface is expected to favor satisfactory cell adhesion, along with proliferation and growth. Whereas the $Ni_{55.6}Ti_{44.4}$ alloy surface having a R_a value lower than 341.69 nm might lead to cell peeling off due to a relatively frail adherence [67].

Further, Fig. 11 (a) reveals similar initial ADSCs adhesion and growth on both surfaces after 4 days of cell culture, which confirmed that the surface milled with cryo-treated cutting during HME favored the initial cell adhesion and growth like CpTi. As stated in the previous sections, the considerably improved topographic features are mostly responsible for fostering improved cell proliferation with adequate cell-cell contact. Additionally, a similar initial ADSCs spread on both surfaces is evident in

Fig. 11 (b), which again validated the non-toxicity and biocompatibility of the HME-milled surface in the initial phase. The initial cell attachment, proliferation, and spreading are decisive for the implant's long-term sustainability and permanence and can vary with the change in biomaterial surface characteristics [68]. Besides, Fig. 11 (c) shows no considerable distinction in cell count between both surfaces. These results indicate that the HME-milled $Ni_{55.6}Ti_{44.4}$ alloy surface promotes similar cell adhesion and proliferation as CpTi, demonstrating that this surface is cytocompatible and promotes cell growth. Additionally, according to Fig. 11 (b), some flatter ADSCs were noticed on the CpTi surface, depicting cell adherence to the CpTi substrate. Whereas a more three-dimensional shape of ADSCs was observed on the HME-milled surface, signaling an assisting physiological attachment. Moreover, in comparison to the smoother cells with certain cellular extensions evident on the CpTi surface, the HME-milled surface was found with the presence of uneven-shaped cellular extensions, appearing to be in a mature state to promote proliferation and differentiation. Thus, the substantial improvements in wetting features, topographic properties, and *in vitro* biological response can altogether claim that the modified $Ni_{55.6}Ti_{44.4}$ alloy surface exhibited promising adequacy of its geometrical characteristics desirable for mechanical interlocking with cells at the micro-level.

4.4 Morphological features of the cryo-treated cutting tool

Fig. 12 demonstrates the wear progression primarily in terms of chipping (chip-flow damage), abrasion grooves (along chip-flow direction), and BUE (adhesion/welding). In Fig. 12 (i), although some parallel abrasion grooves are evident at the top surface, they are not deep enough to cause a major fracture. Further, some of the small chips adhered to some abrasion grooves along with relatively high thermo-mechanical and cyclic stresses [41], which might have also triggered the chipping at the time of pulling off. Since cryogenic cooling promotes the regular formation of tubular chips and opposes the development of lengthy and snarled ones [69], the cutting tool used amid HME plausibly experienced more chipping (due to more cutting tool-chip contact area) than the one used during CME. The sticking or welding of chips on the cutting tool in both Fig. 12 (i) and (ii) confirms the adhesion wear. However, it is found less in the case of CME due to the lowest temperature effect (minimizing the melting of chips). This finding can be attributed to a previous study [69]. Besides, HME's temperature possibly provided the steady state and most durable wear characteristics of the cryo-treated cutting tool, implying its profound influence against sudden tool wear. Therefore, based on such observations and the visual inspection of Fig. 12, it could be hypothesized that a more favorable work hardening took place in the case of HME, leading to relatively less wear than CME.

Further, as shown in Table 2, the cryo-treated cutting tool achieved increased roughness and reduced microhardness values amid CME. The possible reason for this poor performance of the cryo-treated cutting tool during CME is the further increase in its brittleness and hardness (since the cryogenic treatment of this cutting tool had already increased its brittleness and hardness) as a result of experiencing the extremely low temperature (-196 °C) of CME. Moreover, this increased hardness and brittleness of the cryo-treated cutting tool during CME must have resulted in the cutting edge breakage and damage at several places, as shown in the FESEM image of Fig 12 (ii). However, in Fig. 12 (i), the cryo-treated cutting tool used in HME, exhibits considerably less wear through breakage but more via chipping, thus less change in the cutting tool's geometry than CME. Additionally, the higher levels of feed rate and cutting depth contribute to higher cutting tool wear. These observations are in strong agreement with some previous findings [24, 53]. Therefore, this is the credible reason why the poor surface finish was reported in the case of milling the difficult-to-cut $Ni_{55.6}Ti_{44.4}$ alloy by the cryo-treated cutting tool during the lowest-temperature cooling environment (CME), since the damaged/worn-out cutting edge of the tool displays more rubbing action (due to aggressive wear) than cutting action on the surface, and thus, deteriorates the overall surface integrity. However, the cooling temperature of HME was noticed to be favorable for the improved functioning of the cryo-treated cutting tool, and thus, less cutting-edge breakage was observed (in the case of higher feed rate and cutting depth) compared to CME. Hence, a considerable role of the cooling environment in subtractive manufacturing could be witnessed.

5. Conclusions and scope

The present study milled $Ni_{55.6}Ti_{44.4}$ alloy with the assistance of an untreated and cryo-treated coated end mill with three distinct cooling mediums and presented promising findings for biomedical applications. Based on the experimental, statistical, and surface characterization studies, the following conclusions could be summed up:

- The applied modeling and optimization approach achieved the optimal combination of lubri-cooling environment and cutting tool type, leading to observing the optimal levels of cutting conditions improved surface roughness (R_a) and microhardness (MHD) results. Hybrid milling environment (HME) combined with the cryo-treated cutting tool, V_c = 55m/min, f_z = 0.075 mm/tooth, and a_p = 1 mm provided the best R_a and MHD outcomes.
- The obtained models of R_a and MHD presented high data variability accounting, with 0.9725 and 0.9955 of the proportion of variability explanation concerning the input variables' levels.
- As a result of the FESEM, EDS, XRD, DSC, and wettability analyses, the HME-milling-induced plastically deformed layer obtained by the cryo-treated cutting tool, exhibited superior surface roughness (0.21 µm), and microhardness (352.8 HV), uniformity, thickness (60.76 µm) and hydrophobicity (CA: 92 °).
- The noteworthy wetting, topographic, and *in vitro* biological responses displayed by the modified $Ni_{55.6}Ti_{44.4}$ alloy surface might be a promising candidate for $Ni_{55.6}Ti_{44.4}$ alloy orthopedic implants.
- The presence of a notable amount of oxide on the HME-milled surface, as demonstrated by the EDS results, might suggest an improved corrosion resistance of this surface.
- The present study conducted the DSC analysis with a positive range of temperature. However, a negative range of the temperature can be incorporated in the extended study and the effect of the same on

the phase transformation in the sample of interest can be investigated in future research.

- The biocompatibility investigation in the present research assessed a short-term biological response of the HME-milled surface produced by a cryo-treated cutting tool and observed satisfactory cell adhesion and growth. However, a longer biocompatibility study will need to be executed to investigate the long-term biological responses of this surface.
- The HME-milled $Ni_{55.6}Ti_{44.4}$ alloy surface was observed to be as good as CpTi owing to its noteworthy biocompatibility. However, a longer *in vitro* study will need to be conducted in the future to investigate the osteogenic activity properties of this surface.
- The present study presented a brief investigation of the cryo-treated cutting tool wear that occurred amid HME and CME. Future studies are strongly encouraged to fully address a detailed investigation of the wear rate and wear mechanism amid each cooling/machining environment.
- The subsequent future experimental study needs to investigate the effects of cutting forces since the input variables can directly influence the same, leading to potential variations in the surface and cutting tool characteristics.

Acknowledgment

The authors convey their sincere gratitude to Dr. Kimberly Cox-York's laboratory from Colorado State University, Fort Collins, CO, USA, for the kind assistance in carrying out the required biocompatibility study using human ADSCs.

Declaration of interests

The authors declare that they have no known competing financial interests or personal relationships that could have appeared to influence the work reported in this paper.

References

1. Safranski D, Dupont K, Gall K (2020) Pseudoelastic nitinol in orthopaedic applications. Shape Mem Superelasticity 6:332–341. https://doi.org/10.1007/s40830-020-00294-y
2. Cheney D (2018) Elastic orthopedic implant and method of manufacturing thereof. Biomed Enterp USPTO 10117647B2
3. Feeney A, Lucas M (2016) Differential scanning calorimetry of superelastic Nitinol for tunable cymbal transducers. J Intell Mater Syst Struct 27:1376–1387. https://doi.org/10.1177/1045389X15591383
4. Kong MC, Axinte D, Voice W (2011) Challenges in using waterjet machining of NiTi shape memory alloys: an analysis of controlled-depth milling. J Mater Process Technol 211:959–971. https://doi.org/10.1016/j.jmatprotec.2010.12.015
5. Cai C, Liang X, An Q, et al (2021) Cooling/lubrication performance of dry and supercritical CO2-based minimum quantity lubrication in peripheral milling Ti-6Al-4V. Int J Precis Eng Manuf Technol 8:405–421. https://doi.org/10.1007/s40684-020-00194-7

6. Davis R, Singh A, Debnath K, et al (2022) Enhanced micro-electric discharge machining-induced surface modification on biomedical Ti-6Al-4V alloy. J Manuf Sci Eng 144:. https://doi.org/10.1115/1.4053110
7. Davis R, Singh A, Debnath K, et al (2021) Surface modification of medical-grade Ni55.6Ti44.4 alloy via enhanced machining characteristics of Zn powder mixed-µ-EDM. Surf Coatings Technol 425:. https://doi.org/10.1016/j.surfcoat.2021.127725
8. Davis R, Singh A, Jackson MJ, et al (2022) A comprehensive review on metallic implant biomaterials and their subtractive manufacturing. Int J Adv Manuf Technol 120:1473–1530. https://doi.org/10.1007/s00170-022-08770-8
9. Kaynak Y, Taşcıoğlu E, Sharif S, et al (2022) The effect of cooling on machining and phase transformation responses of Ni-rich NiTiHf high-temperature shape memory alloy. J Manuf Process 75:1144–1152. https://doi.org/10.1016/j.jmapro.2022.01.009
10. Kaynak Y, Karaca HE, Jawahir IS (2011) Cryogenic machining of NiTi shape memory alloys. 6th Int Conf Exhib Des Prod Mach Dies/Molds 123–128
11. Zainal Abidin Z, Tarisai Mativenga P, Harrison G (2020) Chilled air system and size effect in micro-milling of nickel−titanium shape memory alloys. Int J Precis Eng Manuf - Green Technol 7:283–297. https://doi.org/10.1007/s40684-019-00040-5
12. Pimenov DY, Mia M, Gupta MK, et al (2021) Improvement of machinability of Ti and its alloys using cooling-lubrication

techniques: a review and future prospect. J Mater Res Technol 11:719–753. https://doi.org/10.1016/j.jmrt.2021.01.031

13. Woodcraft AL (2007) An introduction to cryogenics. Eur Organ Nucl Res Cern
14. Rotella G, Umbrello D (2014) Finite element modeling of microstructural changes in dry and cryogenic cutting of Ti6Al4V alloy. CIRP Ann - Manuf Technol 63:69–72. https://doi.org/10.1016/j.cirp.2014.03.074
15. DellaCorte C (2010) Nickel-titanium alloys for oil-lubricated bearing and mechanical component applications. Proc ASME/STLE Int Jt Tribol Conf 2009, IJTC2009 225–227. https://doi.org/10.1115/IJTC2009-15055
16. Kaynak Y, Karaca HE, Jawahir IS (2015) Cutting speed dependent microstructure and transformation behavior of NiTi alloy in dry and cryogenic machining. J Mater Eng Perform 24:452–460. https://doi.org/10.1007/s11665-014-1247-6
17. Benedicto E, Rubio EM, Aubouy L, Sáenz-Nuño MA (2022) Sustainable lubrication/cooling systems for efficient turning operations of γ-TiAl parts from the aeronautic industry. Int J Precis Eng Manuf - Green Technol. https://doi.org/10.1007/s40684-022-00435-x
18. Koklu U, Coban H (2020) Effect of dipped cryogenic approach on thrust force, temperature, tool wear and chip formation in drilling of AZ31 magnesium alloy. J Mater Res Technol 9:2870–2880. https://doi.org/10.1016/j.jmrt.2020.01.038

19. Koklu U, Kayhanlar H (2022) An Experimental Investigation on Machinability of AZ31B Magnesium Alloy under Dry and Dipped Cryogenic Approaches. J Mater Eng Perform 31:1285–1296. https://doi.org/10.1007/s11665-021-06264-4
20. Al-Ghamdi KA, Iqbal A, Hussain G (2015) Machinability comparison of AISI 4340 and Ti-6Al-4V under cryogenic and hybrid cooling environments: A knowledge engineering approach. Proc Inst Mech Eng Part B J Eng Manuf 229:2144–2164. https://doi.org/10.1177/0954405414548496
21. Schoop J, Sales WF, Jawahir IS (2017) High speed cryogenic finish machining of Ti-6Al4V with polycrystalline diamond tools. J Mater Process Technol 250:1–8. https://doi.org/10.1016/j.jmatprotec.2017.07.002
22. Mahboob Ali MA, Azmi AI, Murad MN, et al (2021) On the effects of bio-based nanolubricants formulation for the turning of Inconel 718. J Brazilian Soc Mech Sci Eng 43:. https://doi.org/10.1007/s40430-021-03285-x
23. Baldin V, da Silva LRR, Davis R, et al (2023) Dry and MQL milling of AISI 1045 steel with vegetable and mineral-based fluids. Lubricants 11:175. https://doi.org/10.3390/lubricants11040175
24. Davis R, Singh A (2020) Tailoring surface integrity of biomedical Mg Alloy AZ31B using distinct end mill treatment conditions and machining environments. J Mater Eng Perform. https://doi.org/10.1007/s11665-020-05203-z
25. Davis R, Singh A (2021) Performance study of cryo-treated end mill

via wet, cryogenic, and hybrid lubri-coolant-milling induced surface integrity of biocompatible Mg alloy AZ91D. Proc Inst Mech Eng Part C J Mech Eng Sci 095440622110171. https://doi.org/10.1177/09544062211017160

26. Davis R, Singh A, Sabino RM, et al (2021) Performance investigation of cryo-treated end Mill on the mechanical and in vitro behavior of hybrid-lubri-coolant-milled Ti-6Al-4V alloy. J Manuf Process 71:472–488. https://doi.org/10.1016/j.jmapro.2021.09.052
27. Yong AYL, Seah KHW, Rahman M (2007) Performance of cryogenically treated tungsten carbide tools in milling operations. Int J Adv Manuf Technol 32:638–643. https://doi.org/10.1007/s00170-005-0379-0
28. Altas E, Erkan O, Ozkan D, Gokkaya H (2022) Optimization of cutting conditions, parameters, and cryogenic heat treatment for surface roughness in milling of NiTi shape memory alloy. J Mater Eng Perform 31:7315–7327. https://doi.org/10.1007/s11665-022-06769-6
29. Kaynak Y, Robertson SW, Karaca HE, Jawahir IS (2015) Progressive tool-wear in machining of room-temperature austenitic NiTi alloys: The influence of cooling/lubricating, melting, and heat treatment conditions. J Mater Process Technol 215:95–104. https://doi.org/10.1016/j.jmatprotec.2014.07.015
30. Kaynak Y (2014) Machining and phase transformation response of room-temperature austenitic NiTi shape memory alloy. J Mater Eng Perform 23:3354–3360. https://doi.org/10.1007/s11665-014-1058-9
31. Kaynak Y, Huang B, Karaca HE, Jawahir IS (2017) Surface

characteristics of machined NiTi shape memory alloy: the effects of cryogenic cooling and preheating conditions. J Mater Eng Perform 26:3597–3606. https://doi.org/10.1007/s11665-017-2791-7

32. Khalil ANM, Azmi AI, Murad MN, Ali MAM (2021) Influence of hybrid cooling-lubricating strategy in the turning of astm f2063 austenitic nickel-titanium alloy. Tribol Ind 43:83–95. https://doi.org/10.24874/ti.1005.11.20.02
33. Otsuka F, Kataoka Y, Miyazaki T (2012) Enhanced osteoblast response to electrical discharge machining surface. Dent Mater J 31:309–315. https://doi.org/10.4012/dmj.2011-039
34. Damiati L, Eales MG, Nobbs AH, et al (2018) Impact of surface topography and coating on osteogenesis and bacterial attachment on titanium implants. J Tissue Eng 9:204173141879069. https://doi.org/10.1177/2041731418790694
35. Tanzi MC, Farè S, Candiani G (2019) Biomaterials and applications. In: Foundations of Biomaterials Engineering. Elsevier, pp 199–287
36. Akincioğlu S, Gökkaya H, Uygur İ (2015) A review of cryogenic treatment on cutting tools. Int J Adv Manuf Technol 78:1609–1627. https://doi.org/10.1007/s00170-014-6755-x
37. Mahendran R, Rajkumar P, Nirmal Raj L, et al (2021) Effect of deep cryogenic treatment on tool life of multilayer coated carbide inserts by shoulder milling of EN8 steel. J Brazilian Soc Mech Sci Eng 43:. https://doi.org/10.1007/s40430-021-03100-7
38. Khanna N, Agrawal C, Pimenov DY, et al (2021) Review on design and development of cryogenic machining setups for heat resistant

alloys and composites. J Manuf Process 68:398–422. https://doi.org/10.1016/j.jmapro.2021.05.053

39. Shokrani A, Al-Samarrai I, Newman ST (2019) Hybrid cryogenic MQL for improving tool life in machining of Ti-6Al-4V titanium alloy. J Manuf Process 43:229–243. https://doi.org/10.1016/j.jmapro.2019.05.006

40. Gajrani KK (2020) Assessment of cryo-MQL environment for machining of Ti-6Al-4V. J Manuf Process 60:494–502. https://doi.org/10.1016/j.jmapro.2020.10.038

41. Kaynak Y, Lu T, Jawahir IS (2014) Cryogenic machining-induced surface integrity: A review and comparison with dry, MQL, and flood-cooled machining. Mach Sci Technol 18:149–198. https://doi.org/10.1080/10910344.2014.897836

42. Nam HG, Yoo CM, Baek SM, et al (2015) Enhancement of mechanical properties and testing of nitinol stents in cerebral aneurysm simulation models. Artif Organs 39:E213–E226. https://doi.org/10.1111/aor.12564

43. de Almeida DA, Sabino RM, Souza PR, et al (2020) Pectin-capped gold nanoparticles synthesis in-situ for producing durable, cytocompatible, and superabsorbent hydrogel composites with chitosan. Int J Biol Macromol 147:138–149. https://doi.org/10.1016/j.ijbiomac.2020.01.058

44. Bombaldi de Souza RF, Bombaldi de Souza FC, Thorpe A, et al (2020) Phosphorylation of chitosan to improve osteoinduction of chitosan/xanthan-based scaffolds for periosteal tissue engineering.

Int J Biol Macromol 143:619–632. https://doi.org/10.1016/j.ijbiomac.2019.12.004

45. Ramin BBS, Rufato KB, Sabino RM, et al (2019) Chitosan/iota-carrageenan/curcumin-based materials performed by precipitating miscible solutions prepared in ionic liquid. J Mol Liq 290:. https://doi.org/10.1016/j.molliq.2019.111199

46. Plath AMS, Facchi SP, Souza PR, et al (2021) Zein supports scaffolding capacity toward mammalian cells and bactericidal and antiadhesive properties on poly(ε-caprolactone)/zein electrospun fibers. Mater Today Chem 20:100465. https://doi.org/10.1016/j.mtchem.2021.100465

47. Kaynak Y, Robertson SW, Karaca HE, Jawahir IS (2015) Progressive tool-wear in machining of room-temperature austenitic NiTi alloys: the influence of cooling/lubricating, melting, and heat treatment conditions. J Mater Process Technol 215:95–104. https://doi.org/10.1016/j.jmatprotec.2014.07.015

48. Lagarde Q, Wagner V, Dessein G, Harzallah M (2021) Effect of temperature on tool wear during milling of Ti64. J Manuf Sci Eng 143:. https://doi.org/10.1115/1.4049847

49. Braghini Junior A, Diniz AE, Filho FT (2009) Tool wear and tool life in end milling of 15-5 PH stainless steel under different cooling and lubrication conditions. Int J Adv Manuf Technol 43:756–764. https://doi.org/10.1007/s00170-008-1744-6

50. Ozturk E, Tunc LT, Budak E (2011) Analytical methods for increased productivity in five-axis ball-end milling. Int J Mechatronics Manuf

Syst 4:238–265. https://doi.org/10.1504/IJMMS.2011.041471

51. Özbek O, Saruhan H (2020) The effect of vibration and cutting zone temperature on surface roughness and tool wear in eco-friendly MQL turning of AISI D2. J Mater Res Technol 9:2762–2772. https://doi.org/10.1016/j.jmrt.2020.01.010
52. Truesdale SL, Shin YC (2009) Microstructural analysis and machinability improvement of Udimet 720 via cryogenic milling. Mach Sci Technol 13:1–19. https://doi.org/10.1080/10910340902776010
53. Altas E, Altin Karatas M, Gokkaya H, Akinay Y (2021) Surface integrity of NiTi shape memory alloy in milling with cryogenic heat treated cutting tools under different cutting conditions. J Mater Eng Perform 30:9426–9439. https://doi.org/10.1007/s11665-021-06095-3
54. Akıncıoğlu S, Gökkaya H, Uygur İ (2016) The effects of cryogenic-treated carbide tools on tool wear and surface roughness of turning of hastelloy C22 based on taguchi method. Int J Adv Manuf Technol 82:303–314. https://doi.org/10.1007/s00170-015-7356-z
55. Kitay O, Kaynak Y (2021) The effect of flood, high-pressure cooling, and CO2-assisted cryogenic machining on microhardness, microstructure, and X-ray diffraction patterns of NiTi shape memory alloy. J Mater Eng Perform 30:5799–5810. https://doi.org/10.1007/s11665-021-05854-6
56. Kaynak Y, Tobe H, Noebe RD, et al (2014) The effects of machining on the microstructure and transformation behavior of NiTi Alloy. Scr Mater 74:60–63. https://doi.org/10.1016/j.scriptamat.2013.10.023

57. Mehrpouya M, Shahedin AM, Daood Salman Dawood S, Kamal Ariffin A (2017) An investigation on the optimum machinability of NiTi based shape memory alloy. Mater Manuf Process 32:1497–1504. https://doi.org/10.1080/10426914.2017.1279290
58. Biermann D, Kahleyss F, Surmann T (2009) Micromilling of NiTi shape-memory alloys with ball nose cutters. Mater Manuf Process 24:1266–1273. https://doi.org/10.1080/10426910903129935
59. Villegas JC, Shaw LL (2009) Nanocrystallization process and mechanism in a nickel alloy subjected to surface severe plastic deformation. Acta Mater 57:5782–5795. https://doi.org/10.1016/j.actamat.2009.08.005
60. Zhao H, Van Humbeeck J, De Scheerder I (2001) Surface conditioning of nickel-titanium alloy stents for improving biocompatibility. Surf Eng 17:451–458. https://doi.org/10.1179/026708401322911356
61. Shabalovskaya S, Anderegg J, Van Humbeeck J (2008) Critical overview of nitinol surfaces and their modifications for medical applications. Acta Biomater 4:447–467. https://doi.org/10.1016/j.actbio.2008.01.013
62. Sullivan SJL, Dreher ML, Zheng J, et al (2015) Effects of oxide layer composition and radial compression on nickel release in nitinol stents. Shape Mem Superelasticity 1:319–327. https://doi.org/10.1007/s40830-015-0028-x
63. Miller DA, Lagoudas DC (2000) Thermomechanical characterization of NiTiCu and NiTi SMA actuators: influence of plastic strains. Smart Mater Struct 9:640–652. https://doi.org/10.1088/0964-1726/9/5/308

64. Moradi S, Hadjesfandiari N, Toosi SF, et al (2016) Effect of extreme wettability on platelet adhesion on metallic implants: from superhydrophilicity to superhydrophobicity. ACS Appl Mater Interfaces 8:17631–17641. https://doi.org/10.1021/acsami.6b03644

65. Menzies KL, Jones L (2010) The impact of contact angle on the biocompatibility of biomaterials. Optom Vis Sci 87:387–399. https://doi.org/10.1097/OPX.0b013e3181da863e

66. Feng CC, Li L, Zhang CS, et al (2019) Surface characteristics and hydrophobicity of Ni-Ti alloy through magnetic mixed electrical discharge machining. Materials (Basel) 12:. https://doi.org/10.3390/ma12030388

67. Stepanovska J, Matejka R, Otahal M, et al (2020) The effect of various surface treatments of Ti6Al4V on the growth and osteogenic differentiation of adipose tissue-derived stem cells. Coatings 10:762. https://doi.org/10.3390/coatings10080762

68. Sabino RM, Mondini G, Kipper MJ, et al (2021) Tanfloc/heparin polyelectrolyte multilayers improve osteogenic differentiation of adipose-derived stem cells on titania nanotube surfaces. Carbohydr Polym 251:. https://doi.org/10.1016/j.carbpol.2020.117079

69. Kaynak Y, Karaca HE, Noebe RD, Jawahir IS (2013) Tool-wear analysis in cryogenic machining of NiTi shape memory alloys: a comparison of tool-wear performance with dry and MQL machining. Wear 306:51–63. https://doi.org/10.1016/j.wear.2013.05.011

Figure

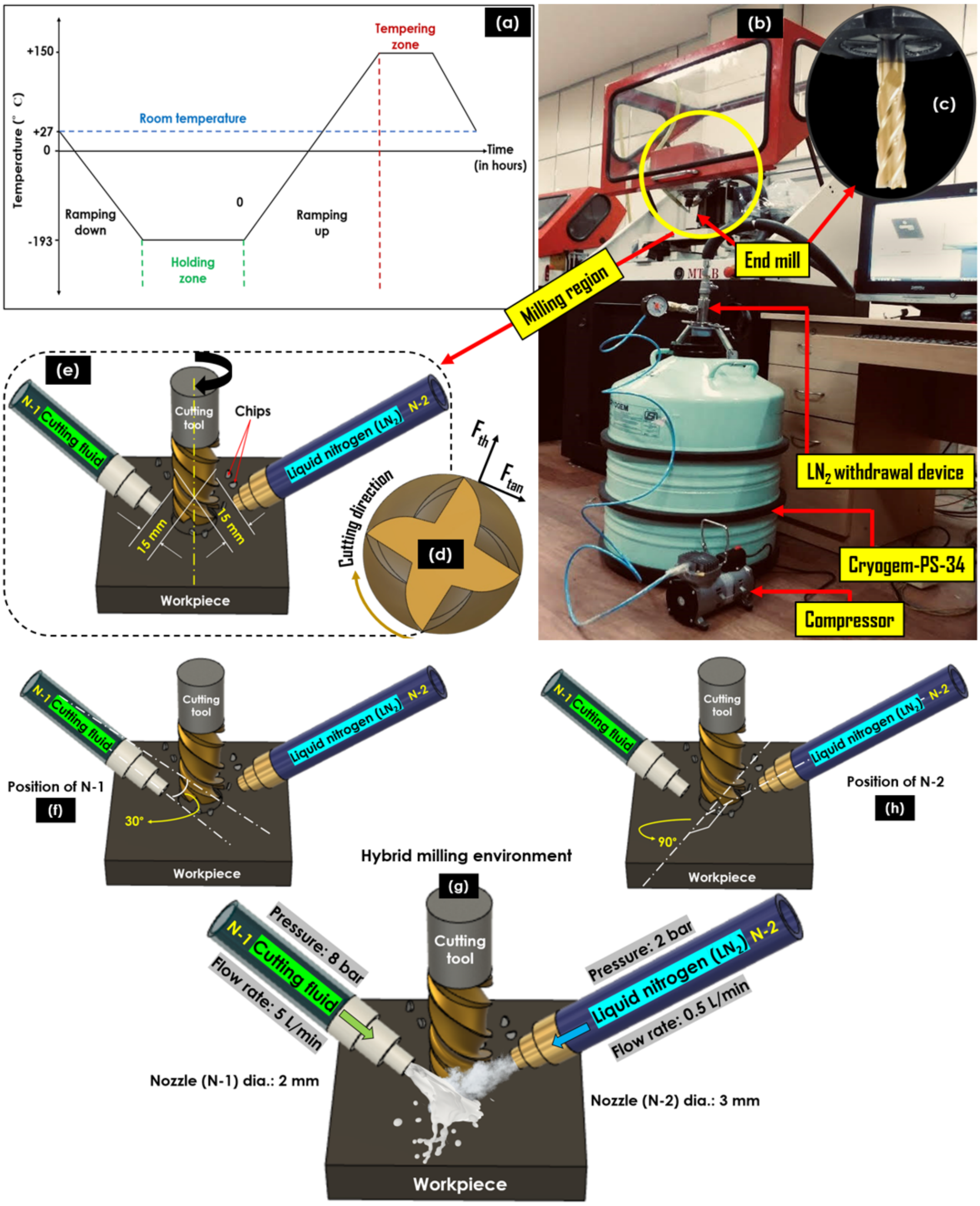

Fig. 1 (a) DCT process, (b) Experimental configuration, (c) End mill cutting tool, (d) Top view of the cutting tool showing thrust force (F_{th}), tangential force (F_{tan}), and cutting direction, (e) Schematic display of stand-off distance of nozzle-1 (N-1) and nozzle-2 (N-2) from cutting tool periphery, (f) position of N-1, (g) hybrid cooling/milling environment (HME), and (h) position of N-2

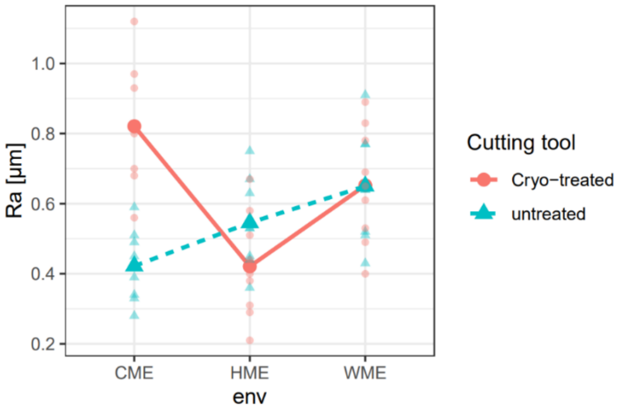

Fig. 2 Mean plot of R_a considering cutting tool and milling environment interactions

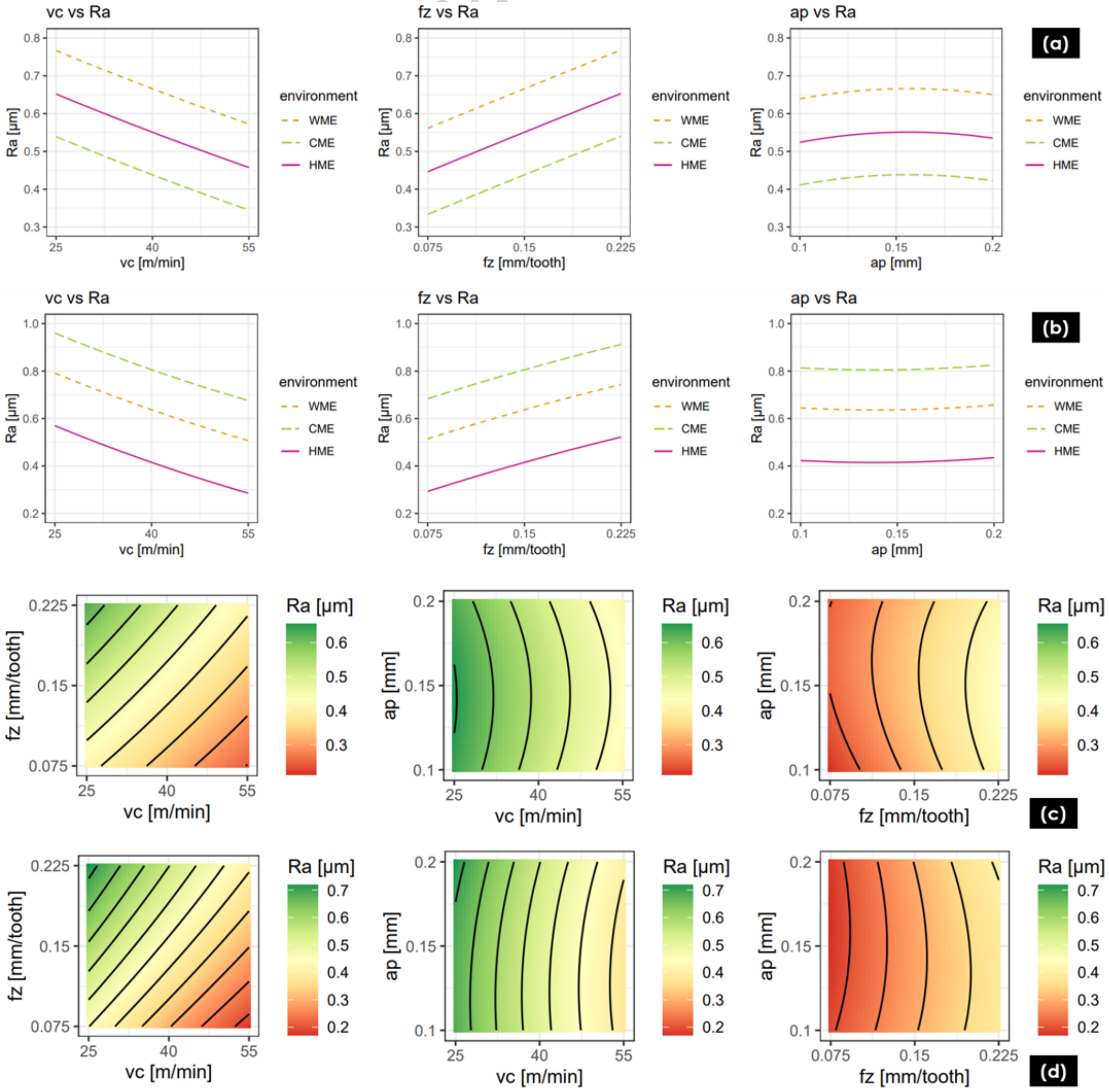

Fig. 3 Effects plot of R_a obtained with (a) untreated and (b) cryo-treated cutting tool; Contour plot of R_a obtained with (c) untreated cutting tool amid CME and (d) cryo-treated cutting tool amid HME

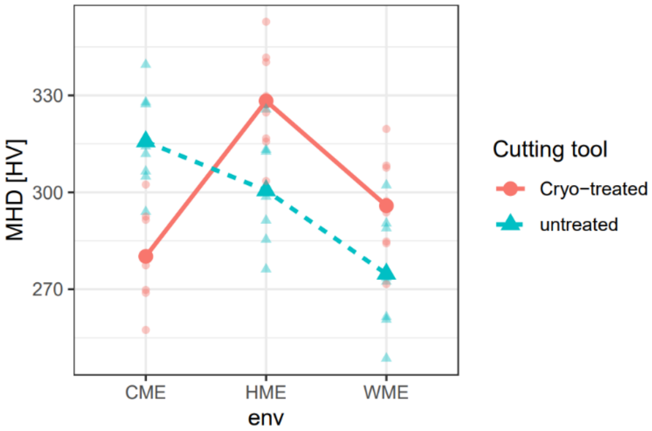

Fig. 4 Mean plot of MHD considering cutting tool and milling environment interactions

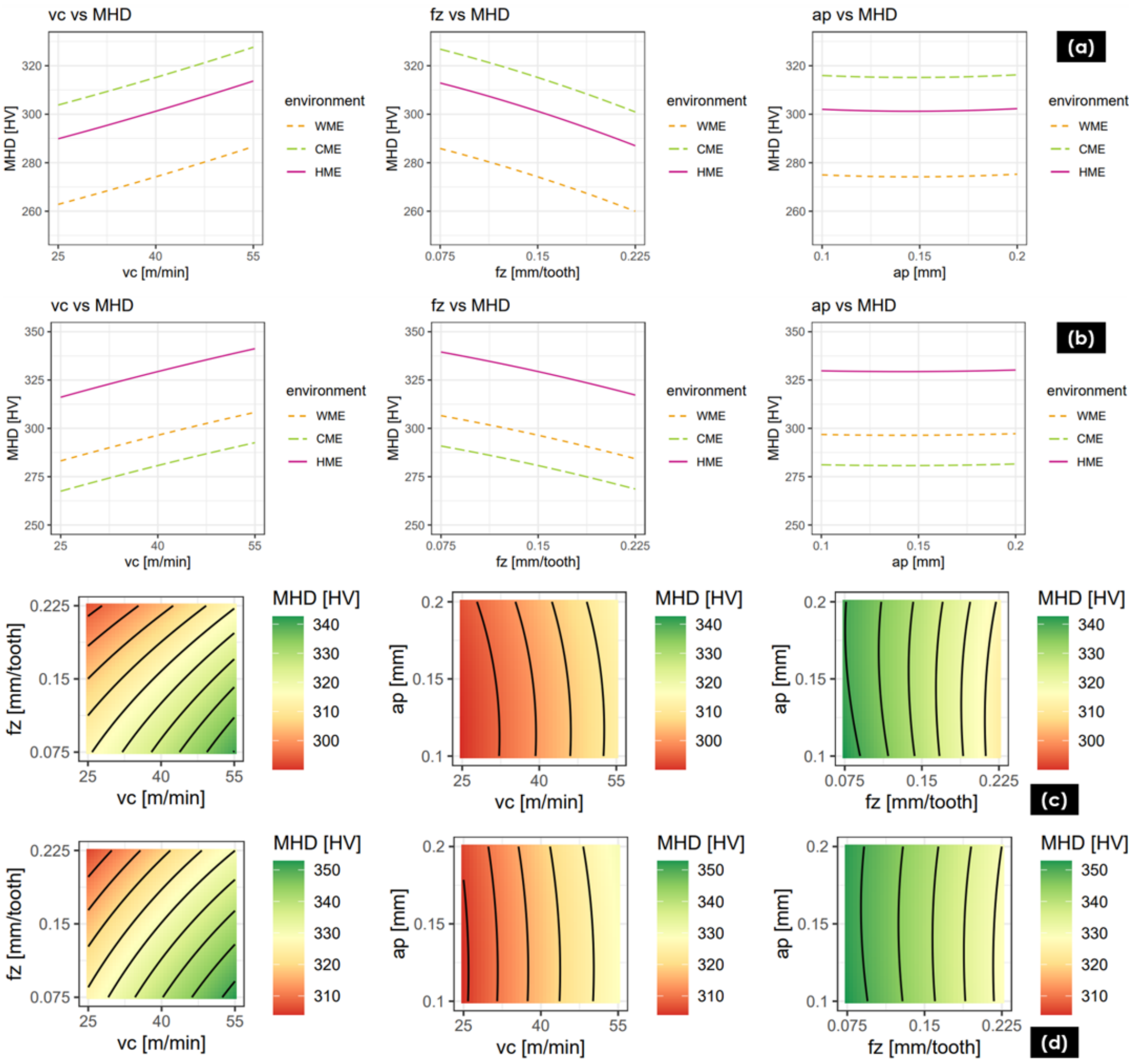

Fig. 5 Effects plot of MHD obtained with (a) untreated and (b) cryo-treated cutting tool; Contour plot of MHD obtained with (c) untreated cutting tool amid CME and (d) cryo-treated cutting tool amid HME

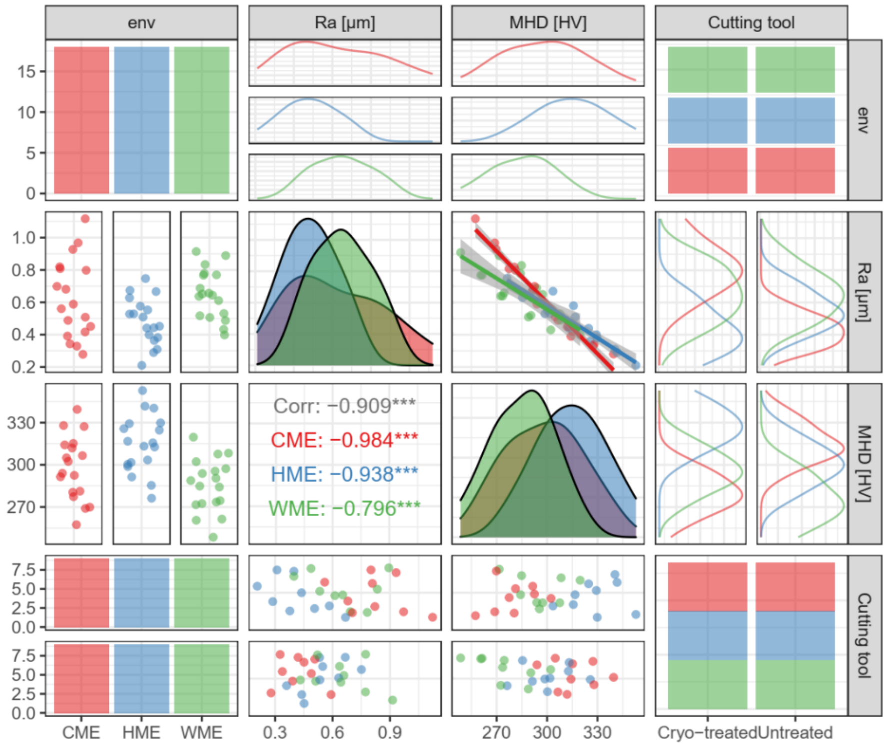

Fig. 6 Pairs plot

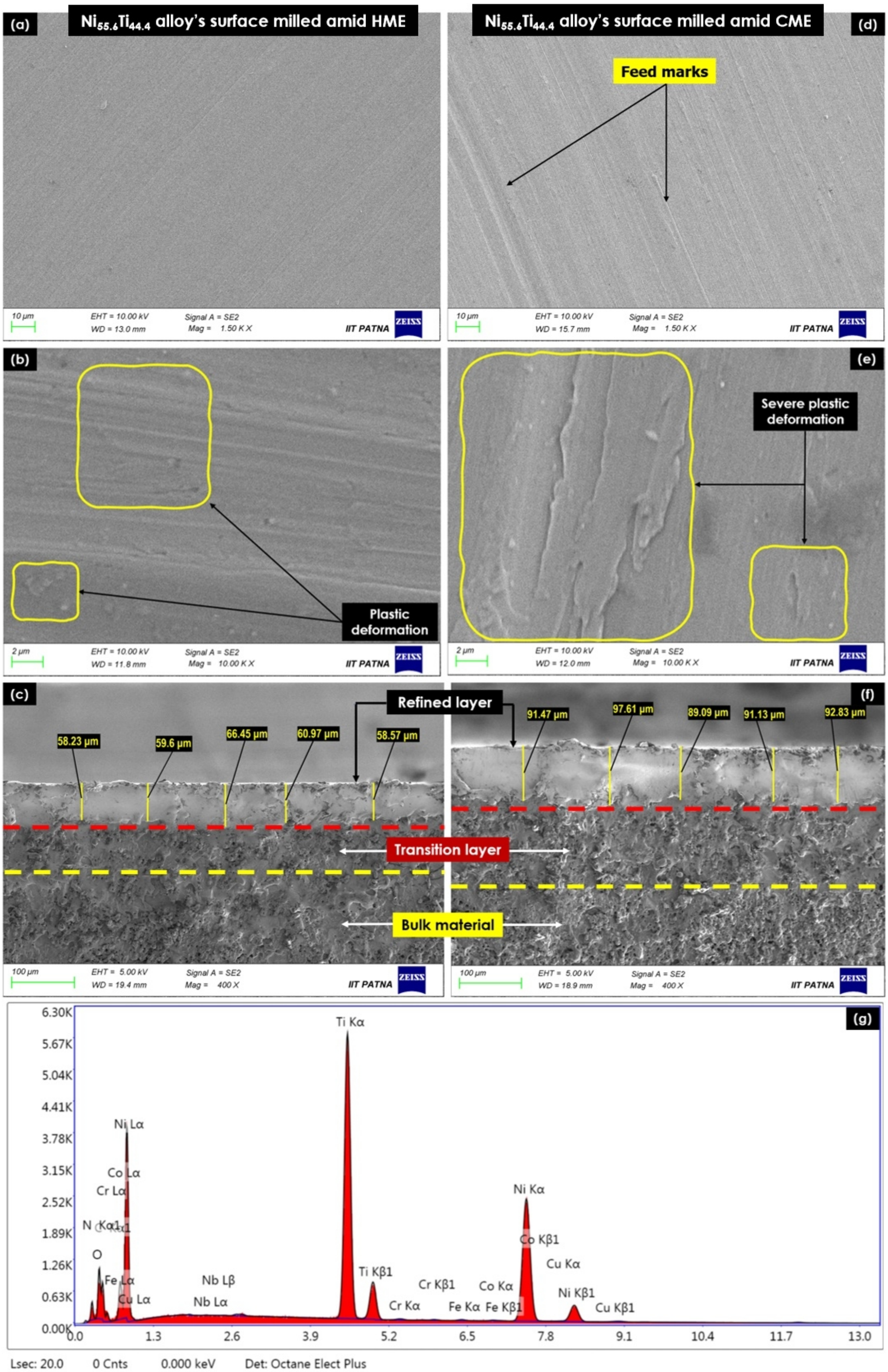

Fig. 7 (a) and (d) Top view at 1.50 K×, (b) and (e) top view at 10 K ×, and (c) and (f) front view at 400 × of the surfaces produced by cryo-

treated cutting tool amid HME and CME, respectively; (g) EDS plot of the surface produced amid HME

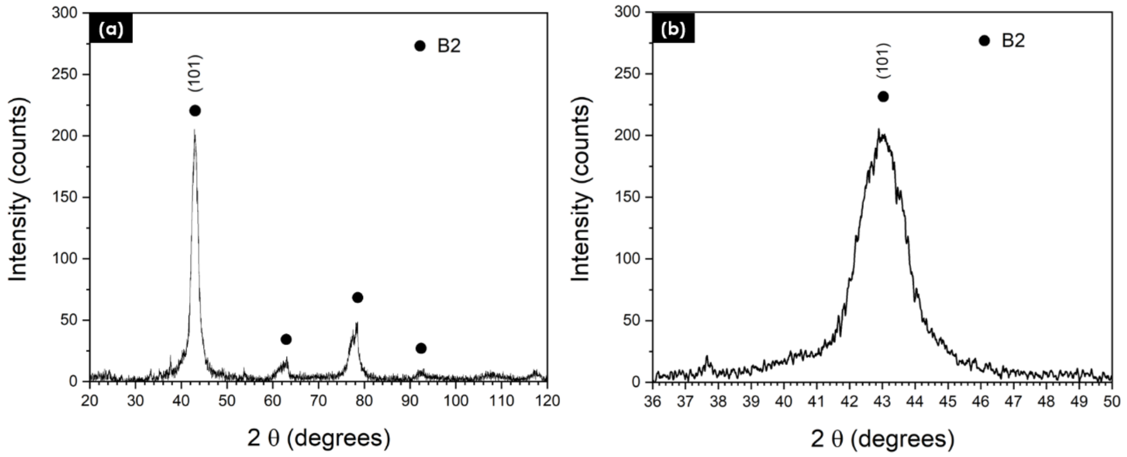

Fig. 8 XRD diffractogram of the HME-milled $Ni_{55.6}Ti_{44.4}$ alloy surface

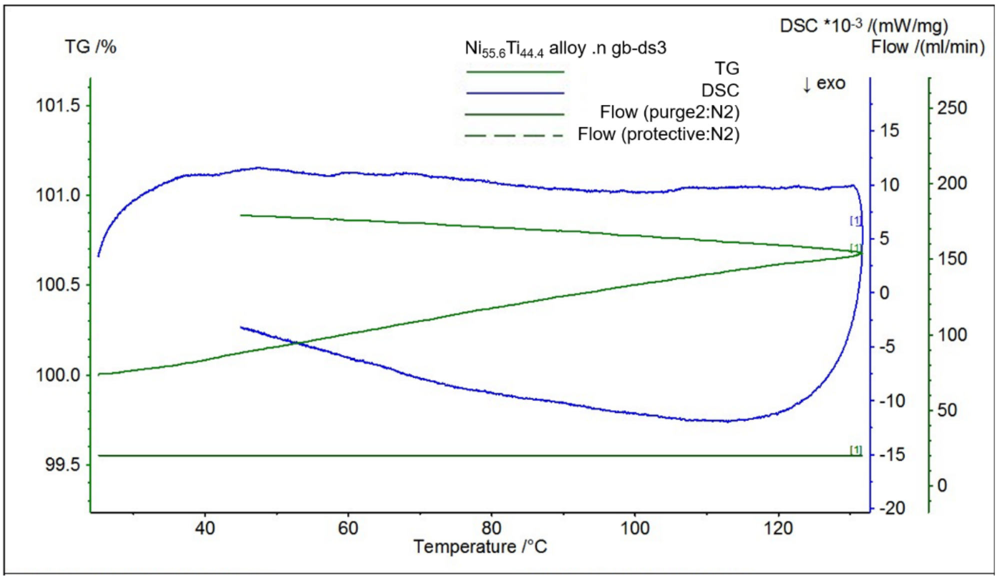

Fig. 9 DSC response of the HME-milled $Ni_{55.6}Ti_{44.4}$ alloy surface

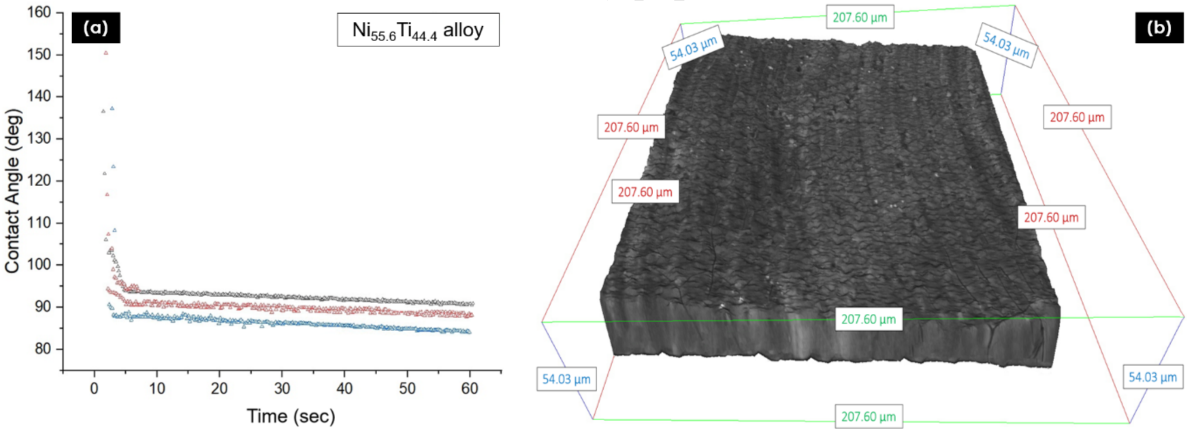

Fig. 10 (a) Static water CAs with respect to time and (b) three-dimensional recreated view for modified $Ni_{55.6}Ti_{44.4}$ alloy surface

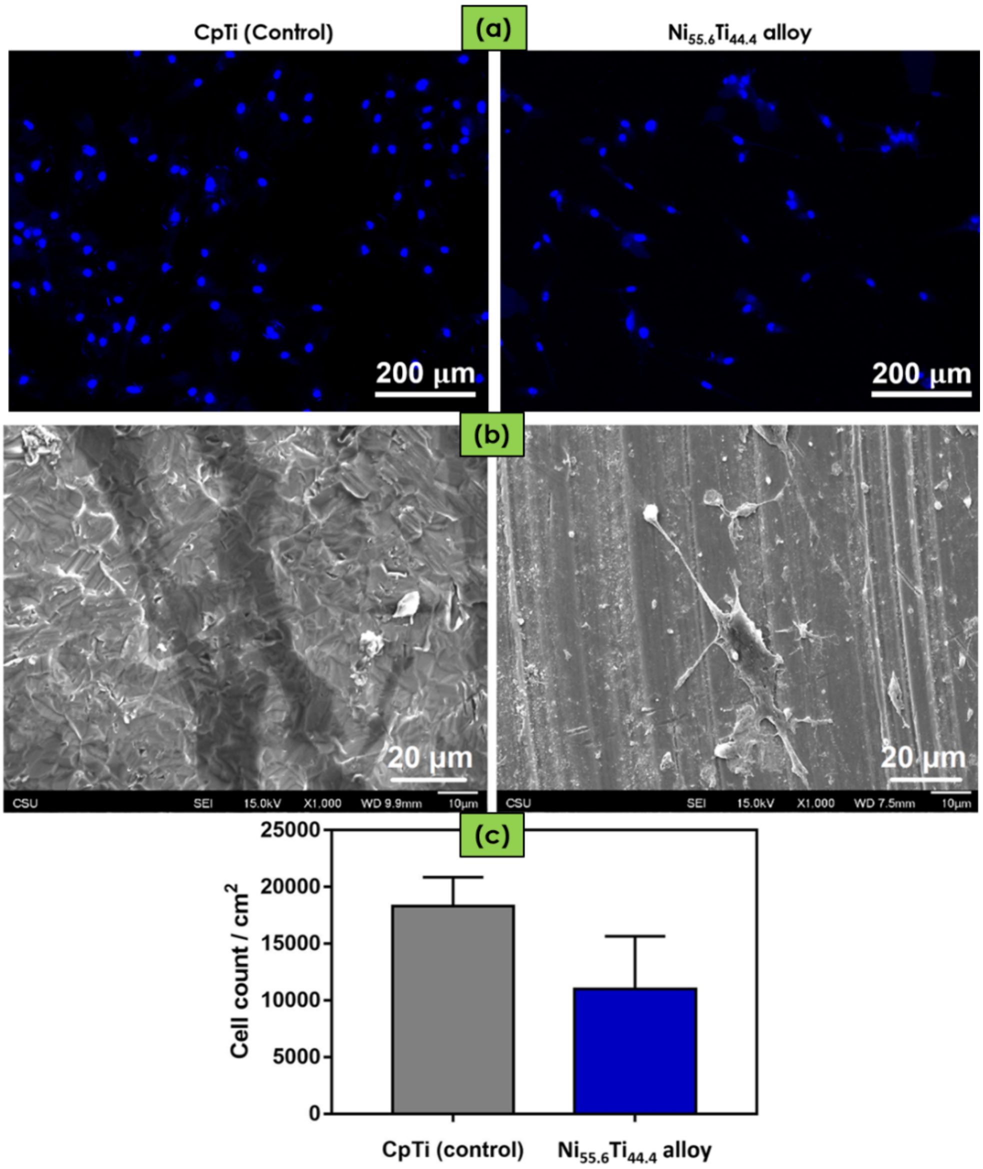

Fig. 11 (a) Fluorescence microscopic images demonstrating ADSCs stained with DAPI (blue) after 4 days of cell culture on both surfaces, (b) SEM images (at 1000× magnification) of ADSCs on both surfaces after 4 days of cell culture, and (c) Cell count per area after 4 days of ADSCs culture. No noticeable distinction in cell count could be noted between the surfaces. The outcomes were statistically analyzed using the Tukey test at a 5% significance level

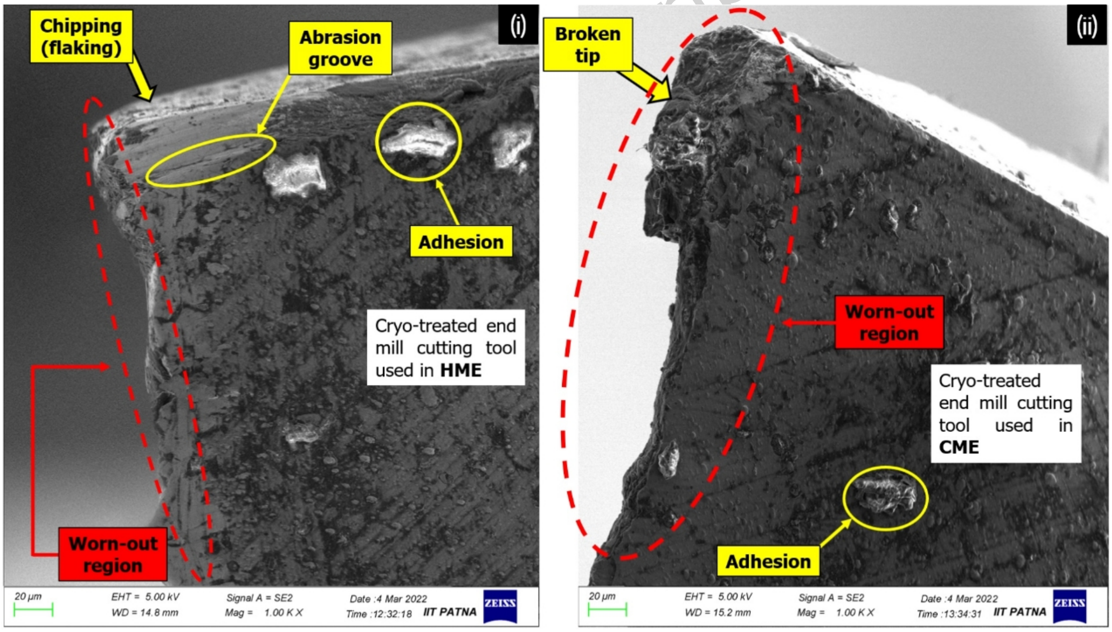

Fig. 12 FESEM images (1000 ×) showing the worn-out and damaged regions (by breakage) on the cutting edges of the cryo-treated cutting tool used in (i) HME and (ii) CME at the optimized setting of input variables

Table

Table 1 Input variables and levels

	Input	unit	Levels		
			-1	0	1
x_1	Cutting-speed (V_c)	m/min	25	40	55
x_2	Feed rate (f_z)	mm/tooth	0.075	0.15	0.225
x_3	Depth of cut (a_p)	mm	1.0	1.5	2.0
x_4	Cutting tool	-	cryo-treated	-	untreated
x_5	Cooling environment (env)	-	WME	HME	CME

Table 2 L27 experimental design and results

Trial run	Input variables				Output variables			
					Untreated cutting tool		Cryo-treated cutting tool	
	V_c (m/min)	f_z (mm/tooth)	a_p (mm)	env	R_a (μm)	MHD (HV)	R_a (μm)	MHD (HV)
1	25	0.075	1.0	WME	0.64	273.6	0.69	293.8
2	25	0.075	1.5	CME	0.39	314.2	0.81	277.4
3	25	0.075	2.0	HME	0.53	301.7	0.44	324.7
4	25	0.150	1.0	CME	0.49	306.5	0.97	268.9
5	25	0.150	1.5	HME	0.67	291.3	0.58	315.7
6	25	0.150	2.0	WME	0.77	261.4	0.83	284.8
7	25	0.225	1.0	HME	0.75	276.2	0.67	303.5
8	25	0.225	1.5	WME	0.91	248.6	0.89	271.6
9	25	0.225	2.0	CME	0.59	294	1.12	257.4
10	40	0.075	1.0	WME	0.51	288.9	0.53	307.6
11	40	0.075	1.5	CME	0.33	327.3	0.68	291.5
12	40	0.075	2.0	HME	0.45	312.6	0.31	340.3
13	40	0.150	1.0	CME	0.42	315.2	0.82	280.5
14	40	0.150	1.5	HME	0.55	300.3	0.4	329.3
15	40	0.150	2.0	WME	0.66	274.5	0.65	297.3
16	40	0.225	1.0	HME	0.63	285.4	0.51	316.7
17	40	0.225	1.5	WME	0.77	260.6	0.78	284.2
18	40	0.225	2.0	CME	0.51	304.9	0.93	269.8
19	55	0.075	1.0	WME	0.43	302.2	0.4	319.6
20	55	0.075	1.5	CME	0.28	339.5	0.56	302.4
21	55	0.075	2.0	HME	0.36	325.7	0.21	352.8
22	55	0.150	1.0	CME	0.34	327.9	0.7	292.5
23	55	0.150	1.5	HME	0.44	313.2	0.29	341.7
24	55	0.150	2.0	WME	0.52	290.4	0.49	308.3
25	55	0.225	1.0	HME	0.53	298.7	0.38	329.8
26	55	0.225	1.5	WME	0.64	272.4	0.61	295.5
27	55	0.225	2.0	CME	0.45	311.9	0.8	281.2

Table 3 Response model of R_a

Term	Estimate	Pr(>|t|)	
Intercept	0.8213	<2.00E-16	***
x_1	-0.1197	<2.00E-16	***
x_2	0.1089	<2.00E-16	***
x_3	0.0058	0.292	
${x_1}^2$	0.0081	0.399	
${x_2}^2$	-0.0044	0.641	
${x_3}^2$	-0.0036	0.705	
env HME	-0.4006	<2.00E-16	***
env WME	-0.1689	1.89E-13	***
untreated cutting tool	-0.3989	<2.00E-16	***
x_1x_2	-0.0108	0.113	
x_1x_3	-0.0008	0.901	
x_2x_3	-0.0006	0.953	
env HME: untreated cutting tool	0.5233	<2.00E-16	***
env WME: untreated cutting tool	0.3967	<2.00E-16	***
R_{adj}^2	0.9725		
Shapiro-wilk	0.8968#		
Breusch-Pagan	0.7271#		

p-values

Signif. codes: 0 ‘***’ 0.001 ‘**’ 0.01 ‘*’ 0.05 ‘.’ 0.1 ‘ ’ 1

Table 4 Response model of MHD

Term	Estimate	Pr(>|t|)	
Intercept	280.188	<2.00e-16	***
x_1	12.2333	<2.00e-16	***
x_2	-12.039	<2.00e-16	***
x_3	0.17222	0.5198	
${x_1}^2$	-0.0778	0.8664	
${x_2}^2$	-1.1444	0.0171	*
${x_3}^2$	0.7722	0.1007	
env HME	48.9694	<2.00e-16	***
env WME	15.6778	<2.00e-16	***
untreated cutting tool	35.5333	<2.00e-16	***
x_1x_2	-0.775	0.0220	*
x_1x_3	-0.0792	0.8087	
x_2x_3	0.86944	0.0658	.
env HME: untreated cutting tool	-63.244	<2.00e-16	***
env WME: untreated cutting tool	-56.656	<2.00e-16	***
R_{adj}^2	0.9955		

Shapiro-wilk	0.6332#
Breusch-Pagan	0.8096#

p-values

Signif. codes: 0 ‘***’ 0.001 ‘**’ 0.01 ‘*’ 0.05 ‘.’ 0.1 ‘ ’ 1